This manuscript was accepted by J. Chem. Phys. Click here to see the version of record.

Nonadiabatic semiclassical dynamics in the mixed quantum-classical initial value representation

Matthew S. Church,[1] Timothy J. H. Hele,[1,2] Gregory S. Ezra,[1] and Nandini Ananth[1,a)]

[1)] *Department of Chemistry and Chemical Biology, Cornell University, Ithaca, New York, 14853, USA*

[2)] *Present address: Cavendish Laboratory, JJ Thomson Avenue, Cambridge University, CB3 0HE, UK*

(Dated: 12 November 2017)

We extend the Mixed Quantum-Classical Initial Value Representation (MQC-IVR), a semiclassical method for computing real-time correlation functions, to electronically nonadiabatic systems using the Meyer-Miller-Stock-Thoss (MMST) Hamiltonian in order to treat electronic and nuclear degrees of freedom (dofs) within a consistent dynamic framework. We introduce an efficient symplectic integration scheme, the MInt algorithm, for numerical time-evolution of the phase space variables and Monodromy matrix under the non-separable MMST Hamiltonian. We then calculate the probability of transmission through a curve-crossing in model two-level systems and show that in the quantum limit MQC-IVR is in good agreement with the exact quantum results, whereas in the classical limit the method yields results in keeping with classical limit approaches like the Linearized Semiclassical IVR. Finally, exploiting the ability of MQC-IVR to quantize different dofs to different extents, we present a detailed study of the extents to which quantizing the nuclear and electronic dofs improves numerical convergence properties without significant loss of accuracy.

[a)] Electronic mail: na346@cornell.edu

This manuscript was accepted by J. Chem. Phys. Click here to see the version of record.

I. INTRODUCTION

The development of theoretical methods for the simulation of electronically nonadiabatic processes remains a central challenge in the effort to understand the mechanisms of photochemical reactions,[1] charge transfer in complex chemical and biological systems,[2–5] and hot-electron generation via inelastic scattering.[6,7]

Over the past two decades, several methods for the simulation of nonadiabatic processes have been developed including exact quantum time-propagation,[8–10] the symmetrical quasi-classical windowing method,[11] mixed quantum-classical Liouville methods,[12–14] and surface hopping.[15–22] In addition, approximate path-integral based methods such as ring polymer molecular dynamics[23–27] and centroid molecular dynamics[28] have also been extended to nonadiabatic systems.[29–38] However, while exact quantum methods are limited to a small number of degrees of freedom (dofs), the more approximate methods fail to capture nuclear quantum coherence effects.

Semiclassical (SC) methods for the calculation of real-time correlation functions, like the Double Herman-Kluk (DHK) Initial Value Representation (IVR),[39–43] accurately describe both electronic and nuclear coherence effects in nonadiabatic systems.[44–49] Unfortunately, much like exact quantum methods, the high computational cost of numerically converging oscillatory integrals has limited these methods to low-dimensional systems. Efforts to mitigate the sign problem have led to the development of more approximate methods such as the linearized (LSC)-IVR[50–53] that fail to capture nuclear quantum coherence effects, and various forward-backward (FB) methods that are either less accurate or computationally expensive.[54–62] The recently-introduced Mixed Quantum-Classical (MQC)-IVR method[63,64] employs a modified Filinov filtration (MFF) scheme[45,63–75] to damp the oscillatory phase of the integrand and has been shown to improve numerical convergence without significant loss of accuracy.[63,64] Specifically, the filtering parameters employed in MQC-IVR modify the extent to which a particular dof contributes to the overall phase of the integrand, effectively controlling the 'quantumness' of that mode.[64]

In this paper we extend MQC-IVR to the simulation of nonadiabatic processes by using the Meyer-Miller-Stock-Thoss (MMST)[76,77] mapping to obtain a continuous Cartesian variable representation of both the electronic and nuclear dofs. We begin by introducing an efficient symplectic integration scheme, the MInt algorithm, for classical trajectory propa-

This manuscript was accepted by J. Chem. Phys. Click here to see the version of record.

gation under the non-separable MMST Hamiltonian. We then calculate the transmission probability using MQC-IVR in a series of model two-level systems with a single curve crossing. We numerically demonstrate that in the limit of a weak filter MQC-IVR agrees well with exact quantum results, and as the filter strength is increased MQC-IVR results start to resemble classical limit methods like the LSC-IVR. We also undertake a systematic investigation of the balance between accuracy and efficiency achieved by quantizing the nuclear and electronic dofs to different extents.

This paper is organized as follows. In section II we briefly review the MQC-IVR theory and provide an overview of the MInt algorithm. Section III describes the model systems studied here and section IV outlines simulation details. Results are discussed in Section V and we present our conclusions in Section VI.

II. THEORY

A. MQC-IVR

The quantum real-time correlation function[78,79] between two operators $\hat{A}$ and $\hat{B}$ is defined as

$$C_{AB}(t) = \mathrm{Tr}\left[\hat{A}e^{\frac{i}{\hbar}\hat{H}t}\hat{B}e^{-\frac{i}{\hbar}\hat{H}t}\right], \tag{1}$$

where $\hat{H}$ is the system Hamiltonian. For the remainder of the paper we use atomic units where $\hbar = 1$. The MQC-IVR correlation function is derived by using the Herman-Kluk (HK-IVR) approximation for the forward and backward time-evolution operators in Eq. (1), followed by a change of variables, and an MFF of the resulting integrand. The final expression is given by[64]

$$\begin{aligned} C_{AB}(t) =& \frac{1}{(2\pi)^{2N}} \int \mathrm{d}\mathbf{z}_0 \int \mathrm{d}\mathbf{z}_0' \ \langle \mathbf{z}_0|\hat{A}|\mathbf{z}_0'\rangle \\ & \times e^{i\left[S_t(\mathbf{z}_0)-S_t(\mathbf{z}_0')\right]} D_t\left(\mathbf{z}_0,\mathbf{z}_0';\mathbf{c},\boldsymbol{\gamma}_0,\boldsymbol{\gamma}_t\right) \\ & \times \langle \mathbf{z}_t'|\hat{B}|\mathbf{z}_t\rangle \, e^{-\frac{1}{2}\boldsymbol{\Delta}_{\mathbf{z}_0}^{\mathrm{T}}\mathbf{c}\boldsymbol{\Delta}_{\mathbf{z}_0}}, \end{aligned} \tag{2}$$

where $\mathbf{z}_0 = (\mathbf{R}_0, \mathbf{x}_0, \mathbf{P}_0, \mathbf{p}_0)$ and $\mathbf{z}_0' = (\mathbf{R}_0', \mathbf{x}_0', \mathbf{P}_0', \mathbf{p}_0')$ are a pair of initial phase space vectors containing both nuclear $(\mathbf{R}, \mathbf{P})$ and electronic $(\mathbf{x}, \mathbf{p})$ variables associated with classical trajectories of length t and action $S_t(\mathbf{z}_0)$ and $S_t(\mathbf{z}_0')$, respectively. The full dimensionality of

This manuscript was accepted by J. Chem. Phys. Click here to see the version of record.

ing system is given by $N = F + G$ where F and G are the dimensionality of the electronic and nuclear phase space vectors, respectively. The phase space displacement between the trajectory pair at time zero is given by $\mathbf{\Delta}_{\mathbf{z}_0} = \mathbf{z}'_0 - \mathbf{z}_0$. The functional form of the prefactor, $D_t\left(\mathbf{z}_0, \mathbf{z}'_0; \mathbf{c}, \boldsymbol{\gamma}_0, \boldsymbol{\gamma}_t\right)$, is provided in Appendix A. The coherent state wavefunctions in momentum and position space are given by

$$\begin{aligned}\langle \tilde{\mathbf{P}}\tilde{\mathbf{p}}|\mathbf{z}_t\rangle = &\left(\frac{1}{\det|\boldsymbol{\gamma}_t|\pi^N}\right)^{\frac{1}{4}} e^{-\frac{1}{2}(\tilde{\mathbf{P}}-\mathbf{P}_t)^{\mathrm{T}}\boldsymbol{\gamma}_t^{-1}(\tilde{\mathbf{P}}-\mathbf{P}_t)-i\tilde{\mathbf{P}}^{\mathrm{T}}\mathbf{R}_t} \\ &\times e^{-\frac{1}{2}(\tilde{\mathbf{p}}-\mathbf{p}_t)^{\mathrm{T}}(\tilde{\mathbf{p}}-\mathbf{p}_t)-i\tilde{\mathbf{p}}^{\mathrm{T}}\mathbf{x}_t}\end{aligned} \tag{3}$$

and

$$\begin{aligned}\langle \tilde{\mathbf{R}}\tilde{\mathbf{x}}|\mathbf{z}_t\rangle = &\left(\frac{\det|\boldsymbol{\gamma}_t|}{\pi^N}\right)^{\frac{1}{4}} e^{-\frac{1}{2}(\tilde{\mathbf{R}}-\mathbf{R}_t)^{\mathrm{T}}\boldsymbol{\gamma}_t(\tilde{\mathbf{R}}-\mathbf{R}_t)+i\mathbf{P}_t^{\mathrm{T}}(\tilde{\mathbf{R}}-\mathbf{R}_t)} \\ &\times e^{-\frac{1}{2}(\tilde{\mathbf{x}}-\mathbf{x}_t)^{\mathrm{T}}(\tilde{\mathbf{x}}-\mathbf{x}_t)+i\mathbf{p}_t^{\mathrm{T}}(\tilde{\mathbf{x}}-\mathbf{x}_t)}\end{aligned} \tag{4}$$

respectively, and the elements of the $G \times G$ diagonal width matrix, $\boldsymbol{\gamma}_t$, determine the spread of the nuclear coherent state in phase space at time t.

The extent of MFF is controlled by the elements of the $2N \times 2N$ diagonal matrix of Filinov parameters,

$$\mathbf{c} = \begin{pmatrix} \mathbf{c}_{\mathbf{q}} & \mathbb{O} \\ \mathbb{O} & \mathbf{c}_{\boldsymbol{\rho}} \end{pmatrix}, \tag{5}$$

where the subscripts $(\mathbf{q}, \boldsymbol{\rho})$ represent the generalized positions and momenta of all N dofs, and $\mathbb{O}$ is the null matrix. The i^{th} diagonal element of the $N \times N$ matrices $\mathbf{c}_{\boldsymbol{\rho}}$ and $\mathbf{c}_{\mathbf{q}}$ regulate momentum and position displacements of the i^{th} dof at time $t = 0$. In the limit $\mathbf{c}_{\boldsymbol{\rho}}, \mathbf{c}_{\mathbf{q}} \to 0$, the MQC-IVR expression reduces to the standard DHK-IVR formulation of the real-time correlation function and in the limit $\mathbf{c}_{\boldsymbol{\rho}}, \mathbf{c}_{\mathbf{q}} \to \infty$, trajectory displacements are constrained to $\mathbf{\Delta}_{\mathbf{z}_0} = \mathbf{0}$, where $\mathbf{0}$ is the null vector, resulting in a classical average,

$$C_{AB}(t) = \frac{1}{(2\pi)^N} \int \mathrm{d}\mathbf{z}_0 \, \langle \mathbf{z}_0|\hat{A}|\mathbf{z}_0\rangle \, \langle \mathbf{z}_t|\hat{B}|\mathbf{z}_t\rangle \,, \tag{6}$$

the Husimi-IVR. By choosing intermediate values of the Filinov parameters for different system modes it is possible to tune the quantumness of individual modes; an optimal choice can significantly accelerate numerical convergence without loss of accuracy.

This manuscript was accepted by J. Chem. Phys. Click here to see the version of record.

B. MMST Hamiltonian and the MInt Algorithm

The MMST Hamiltonian[76,77] for a general F-level system is given by

$$\begin{aligned} H =& \frac{1}{2}\mathbf{P}^{\mathrm{T}}\boldsymbol{\mu}^{-1}\mathbf{P} + \frac{1}{2}\mathbf{p}^{\mathrm{T}}\mathbf{V}(\mathbf{R})\mathbf{p} \\ &+ \frac{1}{2}\mathbf{x}^{\mathrm{T}}\mathbf{V}(\mathbf{R})\mathbf{x} - \frac{1}{2}\mathrm{Tr}\left[\mathbf{V}(\mathbf{R})\right], \end{aligned} \tag{7}$$

where $\mathbf{V}(\mathbf{R})$ is the $F \times F$ diabatic electronic potential energy matrix and $\boldsymbol{\mu}$ is the $G \times G$ diagonal matrix of nuclear masses. The coupling between nuclear positions and the electronic dofs in Eq. (7) makes it challenging to numerically time-evolve classical equations of motion while preserving the symplectic property of Hamiltonian systems.

Here we introduce the MInt algorithm for time evolution under the MMST Hamiltonian in Eq. (7) that exactly conserves total electronic probability (unitarity) and symplecticity independently of time-step size. We provide a detailed study of this algorithm and its properties in Appendix B.

First we establish our notation. Hamiltonian evolution is formally[80]

$$\frac{d}{dt}\mathrm{z} = \mathbf{J}\nabla_{\mathbf{z}}H(\mathbf{z}) \tag{8}$$

where $\mathbf{J}$ is the structure matrix,

$$\mathbf{J} = \begin{pmatrix} \mathbb{O} & \mathbb{I} \\ -\mathbb{I} & \mathbb{O} \end{pmatrix}, \tag{9}$$

and $\mathbb{I}$ is the identity matrix. This is equivalent to use of the Poisson bracket, $\{\cdot, H(\mathbf{z})\}$, since for an arbitrary observable A,

$$\begin{aligned} \frac{d}{dt}A =& (\nabla_{\mathbf{z}}A)^{\mathrm{T}}\frac{d\mathbf{z}}{dt} \\ =& (\nabla_{\mathbf{z}}A)^{\mathrm{T}}\mathbf{J}\nabla_{\mathbf{z}}H(\mathbf{z}) \\ =& \{A, H(\mathbf{z})\}. \end{aligned} \tag{10}$$

In this notation, the Monodromy matrix is given by

$$\mathbf{M} \equiv \frac{d\mathbf{z}_t}{d\mathbf{z}_0}, \tag{11}$$

such that the symplecticity criterion is[80]

$$\mathbf{M}^{\mathrm{T}}\mathbf{J}^{-1}\mathbf{M} = \mathbf{J}^{-1}. \tag{12}$$

We note that this is a stronger condition than conservation of volume in phase space (Liouville's theorem) which only requires $\det|\mathbf{M}| = 1$.

To construct a symplectic method, we exploit the property that exact evolution under a series of sub-Hamiltonians gives approximate evolution under the total Hamiltonian that is exactly symplectic.[80] This scheme is used to construct the conventional Velocity Verlet algorithm and more complicated algorithms[81] such as partitioning the potential energy into fast and slowly-varying components.[79,82] Here, we partition the Hamiltonian in Eq. (7) into two sub-Hamiltonians,

$$H = H_1 + H_2, \tag{13a}$$

$$H_1 = \frac{1}{2}\mathbf{P}^{\mathrm{T}}\boldsymbol{\mu}^{-1}\mathbf{P}, \tag{13b}$$

$$H_2 = \frac{1}{2}\mathbf{p}^{\mathrm{T}}\mathbf{V}(\mathbf{R})\mathbf{p} + \frac{1}{2}\mathbf{x}^{\mathrm{T}}\mathbf{V}(\mathbf{R})\mathbf{x} - \frac{1}{2}\mathrm{Tr}\left[\mathbf{V}(\mathbf{R})\right]. \tag{13c}$$

We then define a flow map, $\Phi_{H_i,t}$, corresponding to exact evolution [Eq. (8)] for timestep t under Hamiltonian H_i. The flow map is simply a function which takes as input phase space coordinates $\mathbf{z}$, and returns the time-evolved values under a specified dynamics. In this notation, exact evolution under the MMST Hamtiltonian is formally $\mathbf{z}_t = \Phi_{H,t}(\mathbf{z}_0)$. We define the MInt algorithm as an approximate flow map, $\Psi_{H,\Delta t}$, which is a series of exact evolutions under the sub-Hamiltonians of Eq. (13b) and Eq. (13c),

$$\Psi_{H,\Delta t} := \Phi_{H_1,\Delta t/2} \circ \Phi_{H_2,\Delta t} \circ \Phi_{H_1,\Delta t/2}, \tag{14}$$

where the circles represent the composition operation: $f \circ g(\mathbf{z}) := f(g(\mathbf{z}))$. In words, Eq. (14) describes time evolution of the system under H_1 for half a time step, under H_2 for a full time step, and under H_1 again for half a time step. As each sub-evolution is symplectic, the total evolution will also be symplectic.[80] To confirm this, in Appendix E we prove symplecticity directly by evaluating Eq. (12) for the MInt algorithm.

We note that while Liouvillians are commonly used to construct symplectic algorithms and to discuss time-evolution in general, exact evolution under a series of Liouvillians is not necessarily symplectic, unless each Liouvillian corresponds to exact evolution under a Hamiltonian.[79,83] For completeness the MInt algorithm is given in the Liouvillian formalism in Appendix D, and compared against a recently-proposed algorithm for evolution under the MMST Hamiltonian[84] that is only symplectic in the limit of an infinitely small time step.

This manuscript was accepted by J. Chem. Phys. Click here to see the version of record.

Evolution under H_1 is free particle motion,

$$\dot{R}_k = \frac{\partial H_1}{\partial P_k} = \frac{P_k}{\mu_{kk}}, \tag{15}$$

for the k^{th} nuclear position coordinate, with all other variables fixed. Integrating Eq. (15) for half a time step, $\Delta t/2$, yields

$$R_k(\Delta t/2) = R_k(0) + \frac{P_k(0)\Delta t}{2\mu_{kk}}. \tag{16}$$

For evolution under H_2,

$$\dot{\mathbf{x}} = \frac{\partial H_2}{\partial \mathbf{p}} = \mathbf{V}(\mathbf{R})\mathbf{p}, \tag{17a}$$

$$\dot{\mathbf{p}} = -\frac{\partial H_2}{\partial \mathbf{x}} = -\mathbf{V}(\mathbf{R})\mathbf{x}, \tag{17b}$$

$$\begin{aligned}\dot{P}_k &= -\frac{\partial H_2}{\partial R_k} \\ &= -\frac{1}{2}(\mathbf{x} - i\mathbf{p})^{\mathrm{T}}\mathbf{V}_k(\mathbf{R})(\mathbf{x} + i\mathbf{p}) \\ &\quad + \frac{1}{2}\mathrm{Tr}\left[\mathbf{V}_k(\mathbf{R})\right],\end{aligned} \tag{17c}$$

with $\mathbf{R}$ fixed, and we define the gradient $\mathbf{V}_k(\mathbf{R}) := \frac{\partial}{\partial R_k}\mathbf{V}(\mathbf{R})$. To solve Eq. (17) we note that $\dot{\mathbf{x}}$ and $\dot{\mathbf{p}}$ are not dependent on $\mathbf{P}$, but $\dot{\mathbf{P}}$ is dependent on $\mathbf{x}$ and $\mathbf{p}$. We can therefore solve for $\mathbf{x}(t)$ and $\mathbf{p}(t)$, $0 \leq t \leq \Delta t$, and substitute this solution into Eq. (17c) to find $\mathbf{P}(\Delta t)$.

The motion of the electronic positions and momenta is therefore given by[10,84]

$$[\mathbf{x}(\Delta t) + i\mathbf{p}(\Delta t)] = e^{-i\mathbf{V}(\mathbf{R})\Delta t}[\mathbf{x}(0) + i\mathbf{p}(0)]. \tag{18}$$

By substituting Eq. (18) into Eq. (17c) we obtain an expression for nuclear momentum evolution:

$$P_k(\Delta t) = P_k(0) - \frac{1}{2}\int_0^{\Delta t} dt\, \left\{[\mathbf{x}(0) - i\mathbf{p}(0)]^{\mathrm{T}} e^{+i\mathbf{V}(\mathbf{R})t}\mathbf{V}_k(\mathbf{R})e^{-i\mathbf{V}(\mathbf{R})t}[\mathbf{x}(0) + i\mathbf{p}(0)] - \mathrm{Tr}[\mathbf{V}_k(\mathbf{R})]\right\}. \tag{19}$$

The above equation can be solved analytically, as discussed in Appendix B. We therefore name the algorithm the MInt algorithm as the nuclear **M**omentum **Int**egral over time in Eq. (19) is solved exactly. In Appendix B we also show how evolution of the Monodromy matrix under $\Psi_{H,\Delta t}$ can be computed exactly. The evolution will be exactly symplectic,

ingisfying Eq. (12) for any time step (although for very large time steps the evolution may become a poor approximation to exact evolution under H).

As discussed further in Appendix C, the MInt algorithm is symmetric and time-reversible, both properties of exact Hamiltonian evolution. Like the Velocity Verlet algorithm, it is second order in time step Δt, and will therefore conserve energy with fluctuations of $\mathcal{O}(\Delta t^2)$ without drifting. The algorithm is also explicit and, being symplectic, automatically satisfies Liouville's theorem. In addition, as noted for exact evolution under the MMST Hamiltonian,[85] the MInt algorithm exactly conserves $\mathcal{G} := \mathbf{x}^{\mathrm{T}}\mathbf{x} + \mathbf{p}^{\mathrm{T}}\mathbf{p}$ and is therefore unitary, i.e. conserves total electronic probability,[85]

$$\sum_{n=1}^{F} \mathcal{P}_n = \frac{1}{2}\sum_{n=1}^{F} x_n^2 + p_n^2 - 1, \tag{20}$$

for any length of time step. It is also invariant to the overall phase (or angle) of the mapping variables, i.e. the transformation

$$(\tilde{\mathbf{x}} + i\tilde{\mathbf{p}}) = e^{-i\theta}(\mathbf{x} + i\mathbf{p}) \tag{21}$$

where θ is a scalar. We note that this algorithm immediately extends to Hamiltonians containing a sum of Meyer-Miller-like terms such as the ring polymer Hamiltonians in Ref. 84.

III. MODEL SYSTEMS

We test MQC-IVR on previously-used model 2-level systems with one nuclear dof.[46] Model 1 has diabatic electronic potential energy matrix elements given by

$$V_{11}(R) = V_0\left(1 + \tanh\left(\alpha_1 R\right)\right) \tag{22a}$$

$$V_{22}(R) = V_0\left(1 - \tanh\left(\alpha_1 R\right)\right) \tag{22b}$$

$$V_{12}(R) = ae^{-bR^2}, \tag{22c}$$

with $V_0 = 0.01$, $\alpha_1 = 1.6$, $a = 0.005$, and $b = 1.0$. Model 2 is an asymmetric version of model 1,

$$V_{11}(R) = V_1\left(1 + \tanh\left(\alpha_2 R\right)\right) \tag{23a}$$

$$V_{22}(R) = V_0\left(1 - \tanh\left(\alpha_2 R\right)\right) \tag{23b}$$

$$V_{12}(R) = ae^{-b(R+f)^2}, \tag{23c}$$

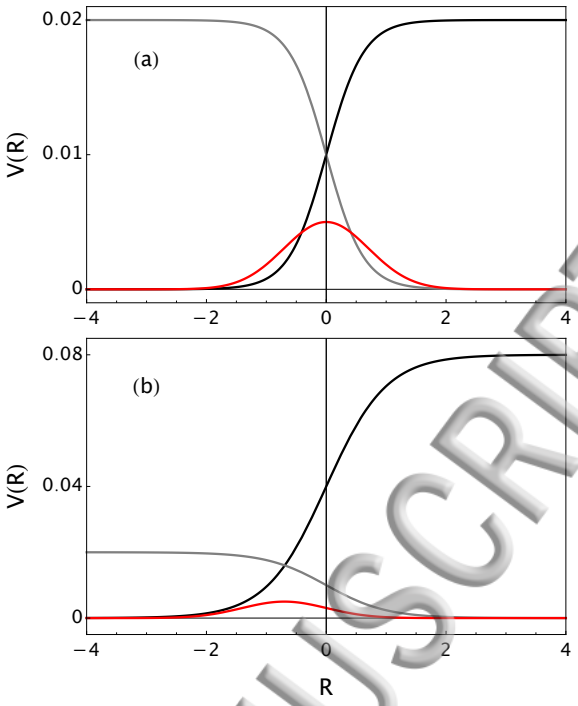

FIG. 1. Elements of the diabatic electronic potential energy matrix for (a) model 1 and (b) model 2 are plotted as a function of the nuclear position: $V_{11}(R)$ (black), $V_{22}(R)$ (grey) and $V_{12}(R)$ (red).

with the same parameters as before and $V_1 = 0.04$, $\alpha_2 = 1.0$, and $f = 0.7$. Plots of the diabats and couplings for each model are provided in Fig. 1.

IV. SIMULATION DETAILS

We compute a real-time correlation function as defined in Eq. (2) for a system initially in a nuclear coherent state occupying electronic state 1. Operator $\hat{A}$ is defined as

$$\hat{A} = |\psi_i\rangle\langle\psi_i| = |P_i R_i 1_1 0_2\rangle\langle P_i R_i 1_1 0_2|\,, \tag{24}$$

where (P_i, R_i) denotes the center of an initial nuclear coherent state. The subscripts of $(1_1, 0_2)$ label the electronic state while a 0 or 1 indicates a ground state or first excited state configuration in the mapping variables corresponding to that state, respectively. The corresponding initial position-space wavefunction is then given by

$$\begin{aligned}\langle R x_1 x_2|\psi_i\rangle = &\left(\frac{\gamma}{\pi}\right)^{\frac{1}{4}} e^{-\frac{\gamma}{2}(R-R_i)^2 + iP_i(R-R_i)} \\ &\times \left(\frac{2}{\pi}\right)^{\frac{1}{2}} x_1 e^{-\frac{1}{2}(x_1^2+x_2^2)},\end{aligned} \tag{25}$$

with $R_i = -5.0$, and the nuclear coherent state width parameter is $\gamma = \gamma_0 = \gamma_t = 0.25$. Simulations are performed with either large incident kinetic energy, 0.1, corresponding to initial nuclear momentum $P_i = 19.9$, or low incident kinetic energy, 0.03, where $P_i = 10.9$. The nuclear mass is 1980.

To compute the particle's distribution of final translational momentum at long times, P_f, we define $\hat{B} = \delta(P_f - \hat{P})$. The MQC-IVR expression for this choice of operators is

$$\begin{aligned} C(P_f) = \lim_{t\to\infty} \frac{1}{(2\pi)^6} \int \mathrm{d}\mathbf{z}_0 \int \mathrm{d}\mathbf{z}_0' \, \langle \mathbf{z}_0|\psi_i\rangle \langle \psi_i|\mathbf{z}_0'\rangle \\ \times e^{i\left[S_t(\mathbf{z}_0) - S_t(\mathbf{z}_0')\right]} D_t(\mathbf{z}_0, \mathbf{z}_0'; \mathbf{c}, \boldsymbol{\gamma}_0, \boldsymbol{\gamma}_t) \\ \times \langle \mathbf{z}_t'|\delta(P_f - \hat{P})|\mathbf{z}_t\rangle \, e^{-\frac{1}{2}\boldsymbol{\Delta}_{\mathbf{z}_0}^{\mathrm{T}} \mathbf{c} \boldsymbol{\Delta}_{\mathbf{z}_0}}. \end{aligned} \tag{26}$$

We choose a nuclear observable for operator $\hat{B}$ rather than, say, electronic state populations because classical limit SC-IVRs generally fail at describing nuclear quantum effects.[46]

For model 1, we sample the initial nuclear coordinates with the following correlated sampling distribution,[86]

$$\begin{aligned} \omega_N(P_0, R_0, P_0', R_0') = & |\langle \bar{P}_0 \bar{R}_0 | P_i R_i\rangle|^2 \\ & \times e^{-\frac{c_P}{2}\Delta_{P_0}^2} e^{-\frac{c_R}{2}\Delta_{R_0}^2}, \end{aligned} \tag{27}$$

where the bars represent mean variables [e.g. $\bar{P}_0 = \frac{1}{2}(P_0' + P_0)$]. The initial coordinates of oscillator 1 are sampled from

$$\begin{aligned} \omega_1(p_{10}, x_{10}, p_{10}', x_{10}') = & |\langle p_{10} x_{10}|1_1\rangle|^2 |\langle p_{10}' x_{10}'|1_1\rangle|^2 \\ & \times e^{-\frac{c_{p10}}{2}\Delta_{p10}^2 - \frac{c_{x10}}{2}\Delta_{x10}^2}, \end{aligned} \tag{28}$$

where the first subscript of the mapping variables indicates the electronic state and the second subscript indicates the time. The initial coordinates of oscillator 2 are sampled from

$$\begin{aligned} \omega_2(p_{20}, x_{20}, p_{20}', x_{20}') = & |\langle p_{20} x_{20}|0_2\rangle|^2 |\langle p_{20}' x_{20}'|0_2\rangle|^2 \\ & \times e^{-\frac{c_{p20}}{2}\Delta_{p20}^2 - \frac{c_{x20}}{2}\Delta_{x20}^2}. \end{aligned} \tag{29}$$

For model 2, we use a different sampling scheme that proves more efficient,

$$\omega(\mathbf{z}_0, \mathbf{z}_0') = |\langle \mathbf{z}_0|\psi_i\rangle \langle \psi_i|\mathbf{z}_0'\rangle| \, e^{-\frac{1}{2}\boldsymbol{\Delta}_{\mathbf{z}_0}^{\mathrm{T}} \mathbf{c} \boldsymbol{\Delta}_{\mathbf{z}_0}}. \tag{30}$$

This manuscript was accepted by J. Chem. Phys. Click here to see the version of record.

The overlap of the coherent states with operator $\hat{B} = \delta(P_f - \hat{P})$ can be found by inserting a momentum identity and using Eq. (3),

$$\begin{aligned}\langle \mathbf{z}'_t|\delta(P_f - \hat{P})|\mathbf{z}_t\rangle &= \left(\frac{1}{\gamma\pi}\right)^{\frac{1}{2}} e^{-\frac{\gamma}{2}(P_f - P'_t)^2} \\ &\times e^{-\frac{\gamma}{2}(P_f - P_t)^2} e^{iP_f(R'_t - R_t)} \\ &\times \prod_{j=1}^{2} e^{-\frac{1}{4}(x'_{jt} - x_{jt})^2 - \frac{1}{4}(p'_{jt} - p_{jt})^2} e^{\frac{i}{2}(p'_{jt} + p_{jt})(x'_{jt} - x_{jt})}.\end{aligned} \tag{31}$$

For both models we use a time step of $\Delta t = 1.5$ a.u. and monitor energy conservation with a tolerance parameter, $\epsilon = 10^{-4}$, such that

$$|1 - E(0)/E(t)| < \epsilon. \tag{32}$$

With the MInt algorithm, we find that only $\sim 0.1\%$ of trajectories violate this tolerance in the model systems presented here and with the time step mentioned above. We use a total simulation time of 3000 a.u. for the high energy simulations and 4000 a.u. for the low energy simulations. We also track the phase of the prefactor in order to select the correct branch of the complex square root. Exact quantum results are obtained by diagonalizing the quantum mechanical Hamiltonian in the Discrete Variable Representation, followed by time-evolution with a Chebyshev propagation algorithm.[46,87]

For all results presented below, we set the position and momentum filtering parameters for a given dof to be equal: $\mathbf{c_q} = \mathbf{c_\rho}$. Further, we take all electronic filtering parameters to be equal, thus treating the two electronic states at the same level of quantization. For clarity, in the rest of this paper, we use c_{nuc} and c_{el} to indicate the values used to filter the nuclear and electronic dofs, respectively.

The SC-Corr code package,[?] developed in-house and available as open-source software, was used to perform the calculations in this study.

V. RESULTS

Here we show the results of using Eq. (26) to compute the particle's distribution of final nuclear momentum after transmission through the curve crossing in models 1 and 2. The MQC-IVR results obtained with model 1 and a high incident energy of 0.1 are shown in Fig. 2. Fig. 3 contains MQC-IVR results obtained with model 2 and an incident energy of

c_{nuc}	c_{el}	N_{traj}	$\max\left[\varepsilon(P_f)\right]$
0.01	0.01	3.2×10^{9}	3.7×10^{-2}
0.05	0.05	5.8×10^{8}	1.1×10^{-1}
0.1	0.1	4.8×10^{8}	1.9×10^{-1}
10.0	10.0	1.5×10^{6}	4.1×10^{-1}
0.01	0.05	7.4×10^{8}	5.1×10^{-2}
0.01	0.1	6.3×10^{8}	8.4×10^{-2}
0.01	10.0	2.4×10^{7}	2.8×10^{-1}
0.05	0.01	1.5×10^{9}	1.1×10^{-1}
0.1	0.01	8.8×10^{8}	1.6×10^{-1}
10.0	0.01	4.8×10^{8}	3.7×10^{-1}

TABLE I. The number of trajectories required for graphical convergence, N_{traj}, of each MQC-IVR result in Fig. 2. Also listed is the absolute error relative to the exact quantum result, as averaged over P_f.

0.1. Fig. 4 and Fig. 5 contain MQC-IVR results obtained with model 2 and a low incident energy of 0.03. All panels show the exact quantum result as a solid black curve.

In Fig. 2(a), Fig. 3(a), Fig. 4(a) and Fig. 4(b), all dofs are equally quantized with $c = c_{\text{nuc}} = c_{\text{el}}$. As expected, the quantum limit filtering strength ($c = 0.01$ shown in pink in the first three figures mentioned) agrees well with the transmission peaks of the exact quantum results, with slight reduction in peak amplitudes and slight broadening of peak widths. The reflection peaks at $P_f = -6.5$ and $P_f = -11.0$ of Fig. 4(a) in this limit, though noisier than the high-intensity transmission peaks, also agree well with the exact quantum result, but with a slight over-estimation of each signal. Increasing the strength of the filter (with $c = 0.05$ and $c = 1.0$ shown in blue and green respectively) in each model further broadens peak widths and reduces peak amplitudes, but the discrete quantum peak structure is retained in each case and significantly fewer trajectories are required for convergence, as reported in Tables I-III. The deviation from exact quantum increases as we further increase filtering strength and, as expected, the MQC-IVR result collapses to the Husimi-IVR result [shown in black, dashed in Fig. 2(a), Fig. 3(a) and Fig. 4(b)] when the filter strength is $c \geq 10$ [shown in red in Fig. 2(a), Fig. 3(a) and Fig. 4(b)].

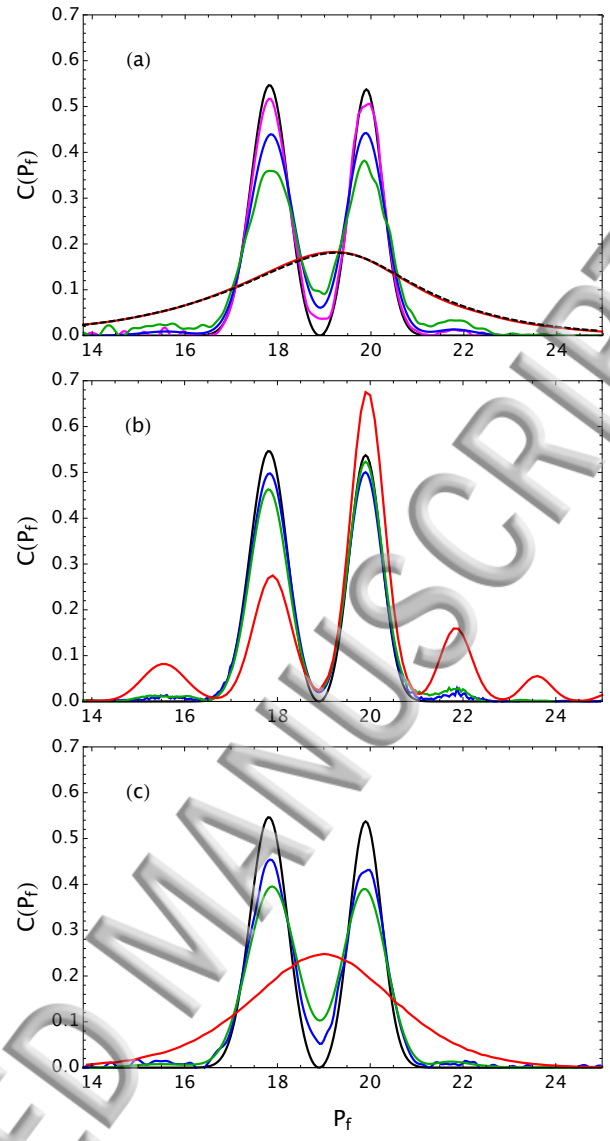

FIG. 2. The distribution of final nuclear momentum with model 1 and an incident energy of 0.1. The exact quantum result (black, solid) is shown in each panel along with (a) the Husimi-IVR (black, dashed) and MQC-IVR where each dof is treated with the same filtering strength: $c = 0.01$ (pink), $c = 0.05$ (blue), $c = 0.1$ (green), and $c = 10.0$ (red); (b) the MQC-IVR results where the nuclear filtering parameters are fixed near the quantum limit, $c_{\text{nuc}} = 0.01$, and the electronic filtering parameters are varied: $c_{\text{el}} = 0.05$ (blue), $c_{\text{el}} = 0.1$ (green), and $c_{\text{el}} = 10.0$ (red); (c) MQC-IVR results where the electronic filtering parameters are fixed near the quantum limit, $c_{\text{el}} = 0.01$, and the nuclear filtering parameters are varied: $c_{\text{nuc}} = 0.05$ (blue), $c_{\text{nuc}} = 0.1$ (green), and $c_{\text{nuc}} = 10.0$ (red).

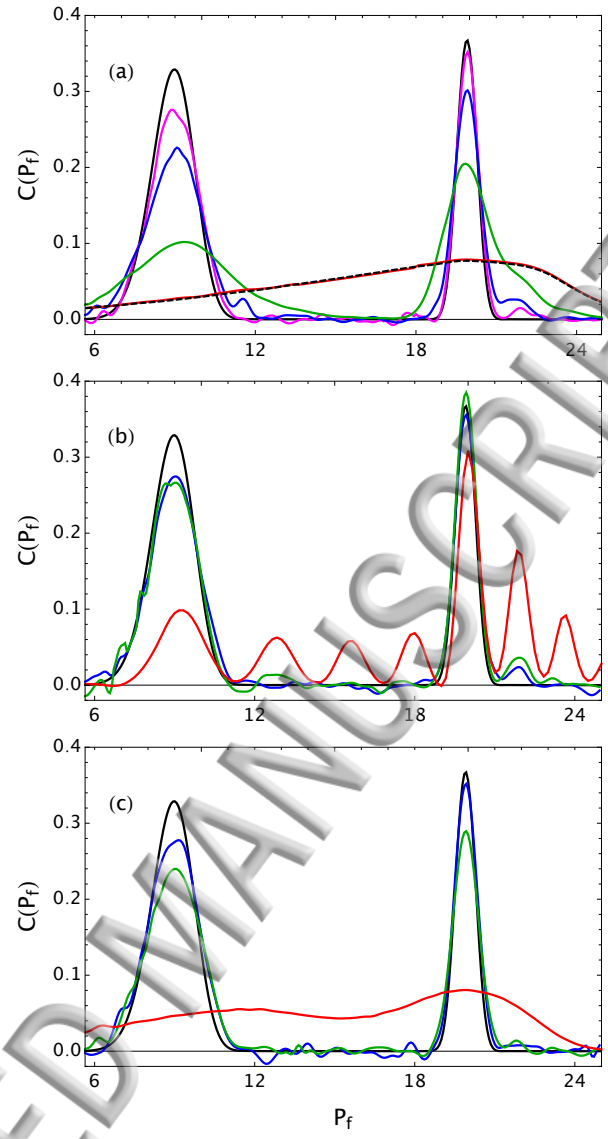

FIG. 3. The distribution of final nuclear momentum with model 2 and incident energy of 0.1. The exact quantum result (black, solid) is shown in each panel along with (a) the Husimi-IVR (black, dashed) and MQC-IVR where each dof is treated with the same filtering strength: $c = 0.01$ (pink), $c = 0.05$ (blue), $c = 0.1$ (green), and $c = 10.0$ (red); (b) the MQC-IVR results where the nuclear filtering parameters are fixed near the quantum limit, $c_{\mathrm{nuc}} = 0.01$, and the electronic filtering parameters are varied from $c_{\mathrm{el}} = 0.05$ (blue) to $c_{\mathrm{el}} = 0.1$ (green) and $c_{\mathrm{el}} = 10.0$ (red); (c) MQC-IVR results where the electronic filtering parameters are fixed in the quantum limit, $c_{\mathrm{el}} = 0.01$, and the nuclear filtering parameters are varied from $c_{\mathrm{nuc}} = 0.05$ (blue) to $c_{\mathrm{nuc}} = 0.1$ (green) and $c_{\mathrm{nuc}} = 10.0$ (red).

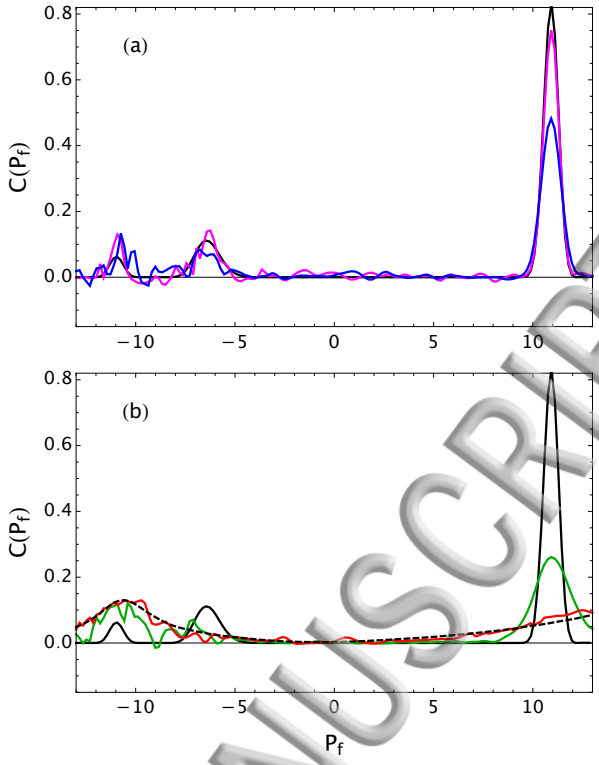

FIG. 4. The final distribution of nuclear momentum with model 2 and an incident energy of 0.03. In both panels the exact quantum result is shown in black along with MQC-IVR results in which each dof is filtered equally: (a) $c = 0.01$ (pink) and $c = 0.1$ (blue); (b) $c = 1.0$ (green) and $c = 10.0$ (red).

We then present MQC-IVR results where the nuclear and electronic dofs are quantized to different extents by varying c_{el} and c_{nuc} independently. In Fig. 2(b), Fig. 3(b), and Fig. 5(a) we fix the nuclear dof in the quantum limit ($c_{\mathrm{nuc}} = 0.01$) and vary the tuning strength associated with the electronic dofs between $c_{\mathrm{el}} = 0.05$ and $c_{\mathrm{el}} = 10.0$. Although the quantum double peak structure is visible in all cases considered here, as we move towards the classical limit ($c_{\mathrm{el}} = 10.0$ shown in red in each case) spurious peaks appear and relative peak intensities change dramatically. We note that, unlike in Fig. 2(a), Fig. 3(a), and Fig. 4(b), where the peaks merge to the mean-field Husimi-IVR result in the classical limit, the discrete peak structure is still visible when only the electronic dofs are treated in the classical limit.

Next, in Fig. 2(c), Fig. 3(c), and Fig. 5(b) we treat the electronic dofs in the quantum limit ($c_{\mathrm{el}} = 0.01$) and vary the extent of nuclear quantization from $c_{\mathrm{nuc}} = 0.01$ to $c_{\mathrm{nuc}} = 10.0$. We find these results are very similar to those in Fig. 2(a), Fig. 3(a), Fig. 4(a), and Fig. 4(b)

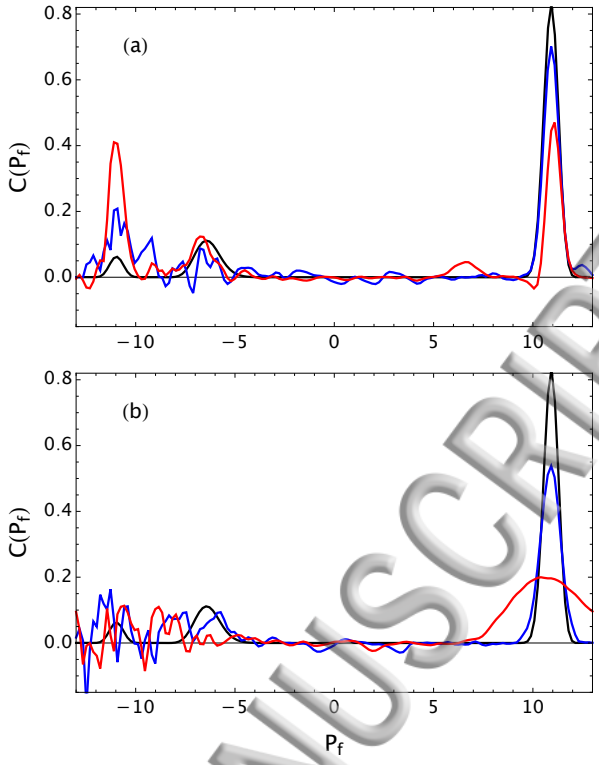

FIG. 5. The final distribution of nuclear momentum with model 2 and an incident energy of 0.03. The exact quantum result is shown in black along with MQC-IVR results where (a) the nuclear filtering parameters are fixed near the quantum limit, $c_{\text{nuc}} = 0.01$, and the electronic dofs are treated with $c_{\text{el}} = 1.0$ (blue) and $c_{\text{el}} = 10.0$ (red); (b) the electronic filtering parameters are fixed near the quantum limit, $c_{\text{el}} = 0.01$, and the nuclear dofs are treated with $c_{\text{nuc}} = 1.0$ (blue) and $c_{\text{nuc}} = 10.0$ (red). The Husimi-IVR result (black, dashed) is also shown in panel (a).

where both electronic and nuclear dofs are equally quantized —the spurious peaks that appear in the cases where the electron dofs are treated in the classical limit do not appear, instead the peaks start to merge with larger c_{nuc}. This gives rise to mean-field like behavior where transmission probability is highest on an unphysical, average electronic surface.

As mentioned above, Tables I-III report the total number of trajectories required for graphical convergence of each MQC-IVR result. Also reported in each table is the maximum absolute error

$$\varepsilon(P_f) = |C_{\text{MQC}}(P_f) - C_{\text{QM}}(P_f)| \tag{33}$$

of each result across all values of P_f. This allows us to clearly identify parameter regimes where the filtering results in improved convergence but little reduction in accuracy. For

c_{nuc}	c_{el}	N_{traj}	$\max\left[\varepsilon(P_f)\right]$
0.01	0.01	1.6×10^{9}	5.7×10^{-2}
0.05	0.05	4.8×10^{8}	1.1×10^{-1}
0.1	0.1	2.8×10^{8}	2.3×10^{-1}
10.0	10.0	3.6×10^{6}	3.1×10^{-1}
0.01	0.05	7.2×10^{8}	5.5×10^{-2}
0.01	0.1	6.0×10^{8}	6.3×10^{-2}
0.01	10.0	1.2×10^{8}	2.4×10^{-1}
0.05	0.01	9.4×10^{8}	5.5×10^{-2}
0.1	0.01	7.2×10^{8}	9.0×10^{-2}
10.0	0.01	4.1×10^{8}	2.9×10^{-1}

TABLE II. The number of trajectories required for graphical convergence, N_{traj}, of each result in Fig. 3. Also listed is the absolute error relative to the exact quantum result, as averaged over P_f.

the high energy simulations with models 1 and 2, an optimal choice of parameters may be $c_{\text{nuc}} = 0.01$ and $c_{\text{el}} = 0.05$ or $c_{\text{el}} = 0.1$ where the number of trajectories required for convergence is on the order of 10^8 with maximum absolute error on the order of 10^{-2}. More trajectories are required in this parameter regime for the low energy simulation of model 2, due to the slower convergence of the reflection peaks, but the number of trajectories required is nearly half that of the weakest filter ($c = 0.01$), and the maximum absolute error only increases from 0.08 to 0.15. We hypothesize that since we are calculating a nuclear observable here, it is necessary to quantize the nuclear dof to a greater extent than the electronic dofs. This idea is further validated by an observation made in the original MQC-IVR implementation[63] for a model 2D adiabatic system of coupled oscillators. Specifically, it was shown that when observing the position of the heavy (more classical mode) it was sufficient to quantize just that mode and the accuracy of the resulting correlation function was largely independent of the extent of quantization used to describe the lighter, unobserved mode.[63]

Although Tables I-III show that the number of trajectories required to converge these low-dimensional model systems is very large, we note that converging the correlation function using quantum limit methods like the DHK-IVR is virtually impossible without MFF or

This manuscript was accepted by J. Chem. Phys. Click here to see the version of record.

c_{nuc}	c_{el}	N_{traj}	$\max\left[\varepsilon(P_f)\right]$
0.01	0.01	3.0×10^{9}	8.0×10^{-2}
0.1	0.1	1.5×10^{9}	3.5×10^{-1}
1.0	1.0	2.6×10^{8}	5.7×10^{-1}
10.0	10.0	2.2×10^{6}	7.5×10^{-1}
0.01	0.1	1.7×10^{9}	1.5×10^{-1}
0.01	10.0	4.5×10^{7}	4.2×10^{-1}
0.1	0.01	2.4×10^{9}	2.9×10^{-1}
10.0	0.01	4.5×10^{8}	6.3×10^{-1}

TABLE III. The number of trajectories required for graphical convergence, N_{traj}, of each result in Fig. 4 and Fig. 5. Also listed is the absolute error relative to the exact quantum result, as averaged over P_f.

other approximations. We also emphasize that as we move to higher dimensional systems, we expect the ability to treat a large number of modes in the classical limit will make the MQC-IVR approach invaluable.

Finally, in Fig. 6 we provide numerical evidence of two important features of the MInt algorithm: symplecticity and energy conservation. We also compare the performance of the MInt algorithm to the non-symplectic, fourth order, Adams-Bashforth predictor-corrector algorithm. Symplecticity is monitored by tracking the element of the matrix

$$\delta\mathbf{M}(t) = \mathbf{M}_{qq}^{\mathrm{T}}\mathbf{M}_{\rho\rho} - \mathbf{M}_{\rho q}^{\mathrm{T}}\mathbf{M}_{q\rho} - \mathbb{I} \tag{34}$$

with the greatest magnitude: a condition derived from Eq. (12). Our energy conservation criterion is

$$\delta E(t) = 1 - E(t)/E(0). \tag{35}$$

In Fig. 6(a), we plot $\delta\mathbf{M}(t)$ along a single low-energy trajectory for model 2 generated using the MInt algorithm, and in Fig. 6(b), we plot $\delta E(t)$. The time range shown along the x-axis corresponds to the time spent by the particle traversing the interaction region and each colored curve represents a different choice of time step ranging from $\Delta t = 0.05$ to $\Delta t = 6.0$. The largest element of $\delta M(t)$ in Fig. 6(a) remains extremely small ($< 10^{-12}$), even for long

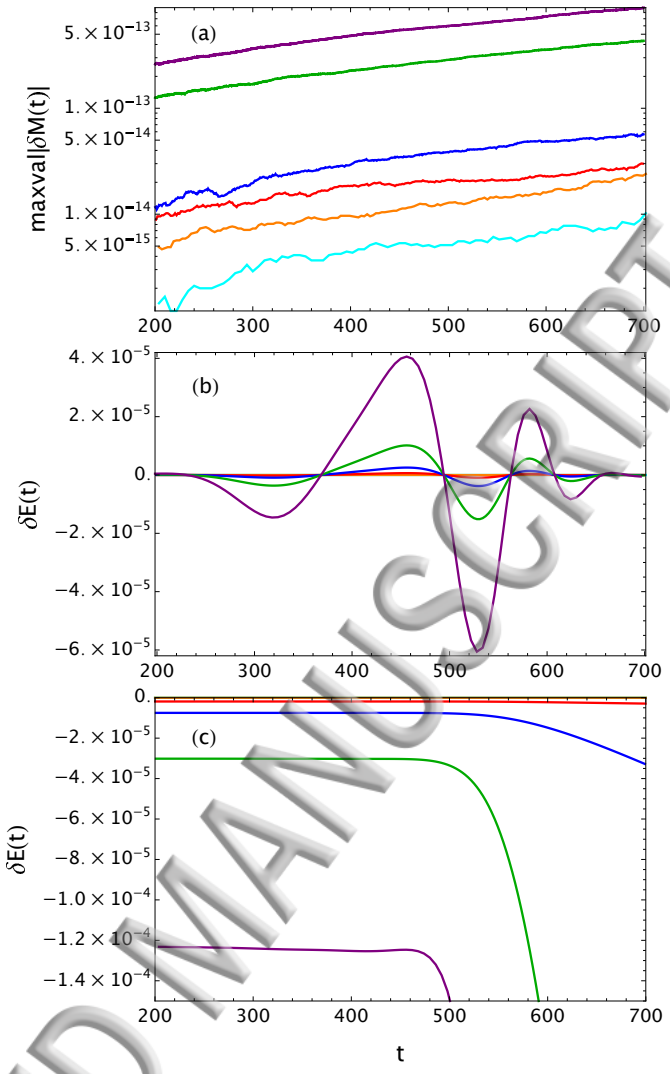

FIG. 6. A plot of (a) the largest element of $\delta\mathbf{M}(t)$ as a function of time as computed with the MInt algorithm, (b) $\delta E(t)$ as a function of time as computed with the MInt algorithm, and (c) $\delta E(t)$ as a function of time as computed with a non-symplectic Adams-Bashforth predictor-corrector algorithm. Each color represents a different time step used: $\Delta t = 0.05$ (cyan), 0.10 (orange), 0.75 (red), 1.5 (blue), 3.0 (green), 6.0 (purple).

times and very coarse time steps, demonstrating that the MInt algorithm is symplectic. The fluctuations in $\delta E(t)$ in Fig. 6(b) oscillate around the true value, and the amplitude of the oscillations decrease with time step size: both characteristics of a symplectic algorithm. Finally, in Fig. 6(c) we plot $\delta E(t)$ for a trajectory with the same initial conditions generated using the fourth order Adams-Bashforth predictor-corrector algorithm. As expected from a non-symplectic integration scheme, the energy drifts away from the true value over time.

VI. CONCLUSIONS

In this article we have successfully extended MQC-IVR to the description of nuclear coherence effects in nonadiabatic systems. We have analyzed the effects of treating both electronic and nuclear dofs under identical and different filtering strengths, and found that there are parameter regimes in both cases which not only reduce computational expense but also maintain a qualitatively accurate description of the transmission through a curve crossing. We also introduced the MInt algorithm for exact symplectic evolution under the MMST Hamiltonian, an important contribution to semiclassical simulations of nonadiabatic processes.

In future work we plan to extend nonadiabatic MQC-IVR to multidimensional nonadiabatic systems such as the NO scattering problem,[6,7] as well as implement the MInt (or similar) algorithm(s) in other nonadiabatic dynamics methods that employ the MMST Hamiltonian.

ACKNOWLEDGEMENTS

The authors acknowledge several helpful discussions with Sergey V. Antipov and his contribution to some of the original code used here. This work was funded, in part, by Army Research Office Grant No. W911NFD-13-1-0102 and an NSF EAGER award No. CHE-1546607. In addition, NA acknowledges funding from the Research Corporation for Science Advancement through a Cottrell Scholar Award, a Sloan Foundation Fellowship, and start-up funding from Cornell University. TJHH acknowledges a Research Fellowship from Jesus College, Cambridge.

Appendix A: MQC-IVR Prefactor

The functional form of the prefactor is given by

$$
\begin{aligned}
D_t\left(\mathbf{z}_0, \mathbf{z}_0'; \mathbf{c}, \boldsymbol{\gamma}_0, \boldsymbol{\gamma}_t\right) \;=\; & \det\left(\frac{1}{2}\boldsymbol{\gamma}_t^{-1}\mathbf{G}\right)^{\frac{1}{2}} \\
& \times \det\Big[\frac{1}{2}(\mathbf{M}^f_{\rho\rho} - i\boldsymbol{\gamma}_t\mathbf{M}^f_{q\rho})(\mathbf{G}^{-1} + \mathbb{I})(\mathbf{M}^b_{\rho\rho}\boldsymbol{\gamma}_t + i\mathbf{M}^b_{\rho q}) \\
& + (\boldsymbol{\gamma}_t\mathbf{M}^f_{qq} + i\mathbf{M}^f_{\rho q})(\frac{1}{2}\boldsymbol{\gamma}_0^{-1} + \mathbf{c}_{\boldsymbol{\rho}})\mathbf{G}^{-1}(\mathbf{M}^b_{\rho\rho}\boldsymbol{\gamma}_t + i\mathbf{M}^b_{\rho q}) \\
& + \frac{1}{2}(\boldsymbol{\gamma}_t\mathbf{M}^f_{qq} + i\mathbf{M}^f_{\rho q})(\mathbf{G}^{-1} + \mathbb{I})(\mathbf{M}^b_{qq} - i\mathbf{M}^b_{q\rho}\boldsymbol{\gamma}_t) \\
& + (\mathbf{M}^f_{\rho\rho} - i\boldsymbol{\gamma}_t\mathbf{M}^f_{q\rho})(\frac{1}{2}\boldsymbol{\gamma}_0 + \mathbf{c}_{\mathbf{q}})\mathbf{G}^{-1}(\mathbf{M}^b_{qq} - i\mathbf{M}^b_{q\rho}\boldsymbol{\gamma}_t)\Big]^{\frac{1}{2}},
\end{aligned}
$$

with diagonal matrix $\mathbf{G} = (\mathbf{c}_{\mathbf{q}} + \boldsymbol{\gamma}_0)\mathbf{c}_{\boldsymbol{\rho}} + \mathbf{c}_{\mathbf{q}}(\boldsymbol{\gamma}_0^{-1} + \mathbf{c}_{\boldsymbol{\rho}})$. We define elements of the unprimed trajectory's monodromy matrix as $\mathbf{M}^f_{\alpha\beta} = \frac{\partial\alpha_t}{\partial\beta_0}$ and the primed trajectory's backward monodromy matrix as $\mathbf{M}^b_{\alpha\beta} = \frac{\partial\alpha_0'}{\partial\beta_t'}$. Note that the backward monodromy matrix is related to its forward counterpart with the following identity,

$$
\mathbf{M}^b \;=\; (\mathbf{M}^{f\prime})^{-1} \;=\; \begin{pmatrix} \mathbf{M}^{f^{\mathrm{T}}\prime}_{\rho\rho} & -\mathbf{M}^{f^{\mathrm{T}}\prime}_{q\rho} \\ -\mathbf{M}^{f^{\mathrm{T}}\prime}_{\rho q} & \mathbf{M}^{f^{\mathrm{T}}\prime}_{qq} \end{pmatrix},
$$

and $\mathbf{M}^{f\prime}_{\alpha\beta} = \frac{\partial\alpha_t'}{\partial\beta_0'}$.

Appendix B: The MInt Algorithm

Here we describe the implementation of the MInt algorithm along with exact evolution of the Monodromy matrix. To avoid computational difficulties with complex numbers the formal evolution equations are rewritten such that the algorithm, when coded, is entirely real.

1. Evolution of positions and momenta

In the following we assume the diabatic electronic potential energy matrix to be real-symmetric; the extension to Hermitian $\mathbf{V}(\mathbf{R})$ is straightforward.

Evolution of nuclear position is given in Eq. (16).

This manuscript was accepted by J. Chem. Phys. Click here to see the version of record.

To evolve the electronic positions and momenta in Eq. (18), we diagonalize the diabatic matrix $\mathbf{V}$ giving eigenvectors $\mathbf{S}$ and a diagonal eigenvalue matrix $\mathbf{\Lambda}$ such that $\mathbf{S}^{\mathrm{T}}\mathbf{V}\mathbf{S} = \mathbf{\Lambda}$, where we drop the $\mathbf{R}$ dependence of $\mathbf{V}$, $\mathbf{S}$, and $\mathbf{\Lambda}$ for clarity. We then calculate

$$\mathbf{C} = \mathbf{S}\cos(\mathbf{\Lambda}\Delta t)\mathbf{S}^{\mathrm{T}} \tag{B1a}$$

$$\mathbf{D} = \mathbf{S}\sin(-\mathbf{\Lambda}\Delta t)\mathbf{S}^{\mathrm{T}} \tag{B1b}$$

such that

$$\mathbf{x}(\Delta t) = \mathbf{C}\mathbf{x}(0) - \mathbf{D}\mathbf{p}(0) \tag{B2a}$$

$$\mathbf{p}(\Delta t) = \mathbf{C}\mathbf{p}(0) + \mathbf{D}\mathbf{x}(0). \tag{B2b}$$

To solve Eq. (19), we insert $\mathbf{S}\mathbf{S}^{\mathrm{T}} = \mathbb{I}$ identities and define

$$\mathbf{W}_k := \mathbf{S}^{\mathrm{T}}\mathbf{V}_k\mathbf{S} \tag{B3}$$

to be the derivative of the potential in the adiabatic basis, giving

$$P_k(\Delta t) = P_k(0) - \frac{1}{2}\int_0^{\Delta t} dt\, \left\{[\mathbf{x}(0) - i\mathbf{p}(0)]^{\mathrm{T}}\mathbf{S}e^{+i\mathbf{\Lambda}t}\mathbf{W}_k e^{-i\mathbf{\Lambda}t}\mathbf{S}^{\mathrm{T}}[\mathbf{x}(0) + i\mathbf{p}(0)] - \mathrm{Tr}[\mathbf{V}_k(\mathbf{R})]\right\}. \tag{B4}$$

As defined earlier we use $\mathbf{V}_k(\mathbf{R}) := \frac{\partial}{\partial R_k}\mathbf{V}(\mathbf{R})$. We then integrate the elements of $e^{+i\mathbf{\Lambda}t}\mathbf{W}_k e^{-i\mathbf{\Lambda}t}$ term by term to give

$$\int_0^{\Delta t} dt\, e^{+i\mathbf{\Lambda}t}\mathbf{W}_k e^{-i\mathbf{\Lambda}t} = \mathbf{\Gamma}_k + i\mathbf{\Xi}_k \tag{B5}$$

where

$$(\mathbf{\Gamma}_k)_{mn} = \begin{cases} (\mathbf{W}_k)_{mn}\,\Delta t & m = n \\ \frac{1}{\lambda_{mn}}\sin(\lambda_{mn}\Delta t)\,(\mathbf{W}_k)_{mn} & m \neq n \end{cases} \tag{B6a}$$

$$(\mathbf{\Xi}_k)_{mn} = \begin{cases} 0 & m = n \\ \frac{1}{\lambda_{mn}}\left[1 - \cos(\lambda_{mn}\Delta t)\right](\mathbf{W}_k)_{mn} & m \neq n \end{cases} \tag{B6b}$$

where we use the shorthand $\lambda_{mn} = (\mathbf{\Lambda})_{mm} - (\mathbf{\Lambda})_{nn}$. Note that $\mathbf{\Gamma}_k$ is real and symmetric and $\mathbf{\Xi}_k$ is real and skew-symmetric since by definition $\lambda_{mn} = -\lambda_{nm}$.

We then rotate $\mathbf{\Gamma}_k$ and $\mathbf{\Xi}_k$ back to the diabatic basis, defining

$$\mathbf{E}_k := \mathbf{S}\mathbf{\Gamma}_k\mathbf{S}^{\mathrm{T}}, \tag{B7a}$$

$$\mathbf{F}_k := \mathbf{S}\mathbf{\Xi}_k\mathbf{S}^{\mathrm{T}}, \tag{B7b}$$

where $\mathbf{E}$ is symmetric and $\mathbf{F}$ is skew-symmetric. Inserting this into Eq. (B4) we finally obtain

$$\begin{aligned} P_k(\Delta t) =& P_k(0) - \frac{1}{2}\{\mathbf{x}^{\mathrm{T}}(0)\mathbf{E}_k\mathbf{x}(0) + \mathbf{p}^{\mathrm{T}}(0)\mathbf{E}_k\mathbf{p}(0) \\ & - 2\mathbf{x}^{\mathrm{T}}(0)\mathbf{F}_k\mathbf{p}(0) - \mathrm{Tr}\left[\mathbf{V}_k\right]\Delta t\}. \end{aligned} \tag{B8}$$

2. Evolution of the monodromy matrix

From Eq. (11), the monodromy matrix in mapping variables is given as

$$\mathbf{M} = \begin{pmatrix} \mathbf{M_{RR}} & \mathbf{M_{Rx}} & \mathbf{M_{RP}} & \mathbf{M_{Rp}} \\ \mathbf{M_{xR}} & \mathbf{M_{xx}} & \mathbf{M_{xP}} & \mathbf{M_{xp}} \\ \mathbf{M_{PR}} & \mathbf{M_{Px}} & \mathbf{M_{PP}} & \mathbf{M_{Pp}} \\ \mathbf{M_{pR}} & \mathbf{M_{px}} & \mathbf{M_{pP}} & \mathbf{M_{pp}} \end{pmatrix} \tag{B9}$$

where

$$\mathbf{M_{XY}} = \frac{\partial \mathbf{X}(t)}{\partial \mathbf{Y}(0)} \tag{B10}$$

for two arbitrary phase space variables $\mathbf{X}$ and $\mathbf{Y}$.

a. *Evolution under* H_1

Since evolution under H_1 is linear, for evolution through $\Delta t/2$ the diagonal elements of $\mathbf{M}$ are unity,

$$\mathbf{M_{RP}} = \frac{\Delta t}{2\mu_{kk}} \tag{B11}$$

and all other elements of $\mathbf{M}$ are zero. The update to the monodromy matrix is therefore[88]

$$\mathbf{M}_{R_k\mathbf{x}}(\Delta t/2) = \mathbf{M}_{R_k\mathbf{x}}(0) + \mathbf{M}_{P_k\mathbf{x}}(0)\frac{\Delta t}{2\mu_{kk}} \tag{B12}$$

and all other elements are unchanged.

b. *Evolution under* H_2

We first observe that for the equations of motion in Eq. (17), $\mathbf{M_{RR}} = \mathbf{M_{PP}} = \mathbb{I}$, and all elements of $\mathbf{M_{Rx}}$, $\mathbf{M_{RP}}$ and $\mathbf{M_{Rp}}$ are zero.

The monodromy matrix elements concerning only the electronic variables can be obtained from Eq. (B2a) and Eq. (B2b) at no extra computational cost,

$$\mathbf{M_{xx}}(\Delta t) = \mathbf{C} \tag{B13a}$$

$$\mathbf{M_{xp}}(\Delta t) = -\mathbf{D} \tag{B13b}$$

$$\mathbf{M_{px}}(\Delta t) = \mathbf{D} \tag{B13c}$$

$$\mathbf{M_{pp}}(\Delta t) = \mathbf{C}. \tag{B13d}$$

We can similarly use Eq. (B8) to determine changes in nuclear momenta with respect to initial electronic coordinates,

$$\mathbf{M}_{P_k\mathbf{x}}(\Delta t) = -\left[\mathbf{x}^{\mathrm{T}}(0)\mathbf{E}_k + \mathbf{p}^{\mathrm{T}}(0)\mathbf{F}_k\right] \tag{B14a}$$

$$\mathbf{M}_{P_k\mathbf{p}}(\Delta t) = -\left[\mathbf{p}^{\mathrm{T}}(0)\mathbf{E}_k - \mathbf{x}^{\mathrm{T}}(0)\mathbf{F}_k\right]. \tag{B14b}$$

Determining $\mathbf{M_{xR}}$ and $\mathbf{M_{pR}}$ requires finding the derivative of a matrix exponential. We use Eq. (B2a) and Eq. (B2b) to give

$$\mathbf{M}_{\mathbf{x}R_k}(\Delta t) = \mathbf{C}_k\mathbf{x}(0) - \mathbf{D}_k\mathbf{p}(0) \tag{B15a}$$

$$\mathbf{M}_{\mathbf{p}R_k}(\Delta t) = \mathbf{C}_k\mathbf{p}(0) + \mathbf{D}_k\mathbf{x}(0), \tag{B15b}$$

where, similar to Appendix A of Ref. 89,

$$\begin{aligned}\mathbf{C}_k :=& \frac{\partial}{\partial R_k}\mathbf{C} \\ =& \mathbf{S}_k \cos(\mathbf{\Lambda}\Delta t)\mathbf{S}^{\mathrm{T}} - \mathbf{S}\sin(\mathbf{\Lambda}\Delta t)\mathbf{\Lambda}_k\Delta t\mathbf{S}^{\mathrm{T}} \\ &+ [\mathbf{S}_k\cos(\mathbf{\Lambda}\Delta t)\mathbf{S}^{\mathrm{T}}]^{\mathrm{T}},\end{aligned} \tag{B16a}$$

$$\begin{aligned}\mathbf{D}_k :=& \frac{\partial}{\partial R_k}\mathbf{D} \\ =& -\mathbf{S}_k\sin(\mathbf{\Lambda}\Delta t)\mathbf{S}^{\mathrm{T}} - \mathbf{S}\cos(\mathbf{\Lambda}\Delta t)\mathbf{\Lambda}_k\Delta t\mathbf{S}^{\mathrm{T}} \\ &- [\mathbf{S}_k\sin(\mathbf{\Lambda}\Delta t)\mathbf{S}^{\mathrm{T}}]^{\mathrm{T}},\end{aligned} \tag{B16b}$$

$$\mathbf{S}_k := \frac{\partial}{\partial R_k}\mathbf{S}, \tag{B16c}$$

$$\mathbf{\Lambda}_k := \frac{\partial}{\partial R_k}\mathbf{\Lambda}. \tag{B16d}$$

For a system with two electronic states $\mathbf{S}_k$ and $\mathbf{\Lambda}_k$ can be determined algebraically, and algorithms exist for finding these exactly for an arbitrary F-level system.[90]

We finally require $\mathbf{M_{PR}}$. Differentiating Eq. (B8) gives

$$\begin{aligned}\mathbf{M}_{P_k R_j} =& -\frac{1}{2}\left[\mathbf{x}^{\mathrm{T}}\mathbf{E}_{jk}\mathbf{x} + \mathbf{p}^{\mathrm{T}}\mathbf{E}_{jk}\mathbf{p} - 2\mathbf{x}^{\mathrm{T}}\mathbf{F}_{jk}\mathbf{p}\right] \\ &+ \frac{1}{2}\mathrm{Tr}\left[\mathbf{V}_{jk}(\mathbf{R})\right]\Delta t, \end{aligned} \tag{B17}$$

where

$$\mathbf{V}_{jk} := \frac{\partial}{\partial R_j}\mathbf{V}_k, \tag{B18a}$$

$$\begin{aligned}\mathbf{E}_{jk} :=& \frac{\partial}{\partial R_j}\mathbf{E}_k \\ =& \mathbf{S}_j\mathbf{\Gamma}_k\mathbf{S}^{\mathrm{T}} + \mathbf{S}\mathbf{\Gamma}_{jk}\mathbf{S}^{\mathrm{T}} + (\mathbf{S}_j\mathbf{\Gamma}_k\mathbf{S}^{\mathrm{T}})^{\mathrm{T}}, \end{aligned} \tag{B18b}$$

$$\begin{aligned}\mathbf{F}_{jk} :=& \frac{\partial}{\partial R_j}\mathbf{F}_k \\ =& \mathbf{S}_j\mathbf{\Xi}_k\mathbf{S}^{\mathrm{T}} + \mathbf{S}\mathbf{\Xi}_{jk}\mathbf{S}^{\mathrm{T}} - (\mathbf{S}_j\mathbf{\Xi}_k\mathbf{S}^{\mathrm{T}})^{\mathrm{T}}, \end{aligned} \tag{B18c}$$

and

$$\begin{aligned}(\mathbf{\Gamma}_{jk})_{mn} :=& \frac{\partial}{\partial R_j}(\mathbf{\Gamma}_k)_{mn} \\ =& \begin{cases} (\mathbf{W}_{jk})_{nm}\Delta t & m = n \\ \frac{1}{\lambda_{mn}}\sin(\lambda_{mn}\Delta t)\left[(\mathbf{W}_{jk})_{mn} - \frac{\lambda_{j,mn}}{\lambda_{mn}}(\mathbf{W}_k)_{mn}\right] + \frac{1}{\lambda_{mn}}\cos(\lambda_{mn}\Delta t)\lambda_{j,mn}\Delta t(\mathbf{W}_k)_{mn} & m \neq n \end{cases}, \end{aligned} \tag{B19a}$$

$$\begin{aligned}(\mathbf{\Xi}_{jk})_{mn} :=& \frac{\partial}{\partial R_j}(\mathbf{\Xi}_k)_{mn} \\ =& \begin{cases} 0 & m = n \\ \frac{1}{\lambda_{mn}}[1-\cos(\lambda_{mn}\Delta t)]\left[(\mathbf{W}_{jk})_{mn} - \frac{\lambda_{j,mn}}{\lambda_{mn}}(\mathbf{W}_k)_{mn}\right] + \frac{1}{\lambda_{mn}}\sin(\lambda_{mn}\Delta t)\lambda_{j,mn}\Delta t(\mathbf{W}_k)_{mn} & m \neq n \end{cases}, \end{aligned} \tag{B19b}$$

and

$$\begin{aligned}\mathbf{W}_{jk} :=& \frac{\partial}{\partial R_j}\mathbf{W}_k \\ =& \mathbf{S}_j^{\mathrm{T}}\mathbf{V}_k\mathbf{S} + \mathbf{S}^{\mathrm{T}}\mathbf{V}_{jk}\mathbf{S} + (\mathbf{S}_j^{\mathrm{T}}\mathbf{V}_k\mathbf{S})^{\mathrm{T}}, \end{aligned} \tag{B20a}$$

$$\lambda_{j,mn} := \frac{\partial}{\partial R_j}\lambda_{mn} = (\mathbf{\Lambda}_j)_{mm} - (\mathbf{\Lambda}_j)_{nn}. \tag{B20b}$$

This manuscript was accepted by J. Chem. Phys. Click here to see the version of record.

Despite the apparent complexity of the monodromy matrix calculations, many terms can be 'recycled' from previous operations, such as matrices $\mathbf{S}$, $\mathbf{C}$ and $\mathbf{D}$, etc. In addition, for a two-level system $\mathbf{S}_j\mathbf{\Xi}_k\mathbf{S}^{\mathrm{T}}$ is diagonal and therefore $\mathbf{F}_{jk} = \mathbf{S}\mathbf{\Xi}_{jk}\mathbf{S}^{\mathrm{T}}$.

3. Complete algorithm

The trajectory is initialized with given values of $\{\mathbf{R}, \mathbf{x}, \mathbf{P}, \mathbf{p}\}$ and $\mathbf{M}(0) = \mathbb{I}$. Starred items are only required if the monodromy matrix is also to be evaluated.

For each time step:

1. Evolve nuclear positions with Eq. (16) for $\Delta t/2$.
2. *Evolve $\mathbf{M}$ for $\Delta t/2$ using Eq. (B12).
3. Compute $\mathbf{V}$ and $\mathbf{V}_k$ $\forall$ k. Diagonalize $\mathbf{V}$ to find $\mathbf{S}$ and $\mathbf{\Lambda}$.
4. Find $\mathbf{C}$ and $\mathbf{D}$ using Eq. (B1) and calculate $\mathbf{x}(t)$ and $\mathbf{p}(t)$ from Eq. (B2).
5. For each k, find $\mathbf{W}_k$ and from it $\mathbf{\Gamma}_k$ and $\mathbf{\Xi}_k$ using Eq. (B6). From these obtain $\mathbf{E}_k$ and $\mathbf{F}_k$ $\forall k$ using Eq. (B7). Therefore find $\mathbf{P}(t)$ from Eq. (B8).
6. *Find $\mathbf{V}_{jk}$, $\mathbf{S}_j$, and $\mathbf{\Lambda}_{jk}$ $\forall$ j, k.
7. *Populate $\mathbf{M}_{\mathbf{xx}}$, $\mathbf{M}_{\mathbf{xp}}$, $\mathbf{M}_{\mathbf{px}}$, and $\mathbf{M}_{\mathbf{pp}}$ from Eq. (B13) using the $\mathbf{C}$ and $\mathbf{D}$ from step 4.
8. *From Eq. (B14) find $\mathbf{M}_{\mathbf{Px}}$ and $\mathbf{M}_{\mathbf{Px}}$ using $\{\mathbf{E}_k\}$ and $\{\mathbf{F}_k\}$ from step 5.
9. *Find $\{\mathbf{C}_k\}$ and $\{\mathbf{D}_k\}$ from Eq. (B16) and therefore $\mathbf{M}_{\mathbf{xR}}$ and $\mathbf{M}_{\mathbf{pR}}$ from Eq. (B15).
10. *Find $\{\mathbf{W}_{jk}\}$ and $\{\lambda_{j,mn}\}$ defined in Eq. (B20) and compute $\mathbf{\Gamma}_{jk}$ and $\mathbf{\Xi}_{jk}$ using Eq. (B19). From these find $\{\mathbf{E}_{jk}\}$ and $\{\mathbf{F}_{jk}\}$ [Eq. (B18)] and compute $\mathbf{M}_{\mathbf{PR}}$ using Eq. (B17).
11. *Evolve the monodromy matrix using the monodromy matrix for $\Phi_{H_2,\Delta t}$ obtained from steps 6 to 10.
12. Repeat steps 1 and 2* for evolution step $\Phi_{H_1,\Delta t/2}$.

We note that a different flow map constructed by swapping H_1 and H_2 in Eq. (14) would also result in a symplectic transformation, but the flow map defined in Eq. (14) requires fewer mathematical operations.

Appendix C: Algorithm properties

A symmetric algorithm is formally defined as[80]

$$\Psi_{-\Delta t} = \Psi_{\Delta t}^{-1}. \tag{C1}$$

To prove this, we use the property that exact evolution under any Hamiltonian is symmetric[80] ($\Phi_t^{-1} = \Phi_{-t}$) and therefore

$$\begin{aligned}\Psi_{H,\Delta t}^{-1} =& \Phi_{\Delta t/2,H_1}^{-1} \circ \Phi_{\Delta t,H_2}^{-1} \circ \Phi_{\Delta t/2,H_1}^{-1} \\ =& \Phi_{-\Delta t/2,H_1} \circ \Phi_{-\Delta t,H_2} \circ \Phi_{-\Delta t/2,H_1} \\ =& \Psi_{H,-\Delta t}\end{aligned} \tag{C2}$$

as required.

Time reversibility is formally[80]

$$\Psi_{H,\Delta t} = \mathbf{\Sigma}\Psi_{H,\Delta t}^{-1}(\mathbf{\Sigma z}) \tag{C3}$$

where the involution $\mathbf{\Sigma}$ is

$$\mathbf{\Sigma} = \begin{pmatrix} \mathbb{I} & \mathbf{0} \\ \mathbf{0} & -\mathbb{I} \end{pmatrix}. \tag{C4}$$

Exact evolution under the MMST Hamiltonian is time reversible since $H(\mathbf{R}, \mathbf{x}, \mathbf{P}, \mathbf{p}) = H(\mathbf{R}, \mathbf{x}, -\mathbf{P}, -\mathbf{p})$. This can be proven for $\Psi_{H,\Delta t}$ since exact evolution under H_1 and H_2 is time-reversible and therefore

$$\begin{aligned}\mathbf{\Sigma}\Psi_{H,\Delta t}^{-1}(\mathbf{\Sigma z}) =& \mathbf{\Sigma}[\Phi_{\Delta t/2,H_1} \circ \Phi_{\Delta t,H_2} \circ \Phi_{\Delta t/2,H_1}]^{-1}(\mathbf{\Sigma z}) \\ =& \mathbf{\Sigma}\Phi_{\Delta t/2,H_1}^{-1} \circ \Phi_{\Delta t,H_2}^{-1} \circ \Phi_{\Delta t/2,H_1}^{-1}(\mathbf{\Sigma z}) \\ =& \mathbf{\Sigma}\Phi_{\Delta t/2,H_1}^{-1} \circ \Phi_{\Delta t,H_2}^{-1}[\mathbf{\Sigma}\Phi_{\Delta t/2,H_1}(\mathbf{z})] \\ =& \mathbf{\Sigma}\Phi_{\Delta t/2,H_1}^{-1}[\mathbf{\Sigma}\Phi_{\Delta t,H_2} \circ \Phi_{\Delta t/2,H_1}(\mathbf{z})] \\ =& \Phi_{\Delta t/2,H_1} \circ \Phi_{\Delta t,H_2} \circ \Phi_{\Delta t/2,H_1}(\mathbf{z}) \\ =& \Psi_{\Delta t}(\mathbf{z}).\end{aligned} \tag{C5}$$

To show that the algorithm is second order, one can write out exact evolution under H in powers of Δt using the Liouvillian formalism and then compare to evolution under $\Psi_{H,\Delta t}$, noting that terms differ at $\mathcal{O}(\Delta t^3)$. More elegantly, since a method constructed by Hamiltonian splitting is exactly symplectic and at least first order,[80] and that a symmetric method has to be of even order,[80] the algorithm must be (at least) second order accurate.

To prove that $\mathcal{G} := \mathbf{x}^{\mathrm{T}}\mathbf{x} + \mathbf{p}^{\mathrm{T}}\mathbf{p}$ is conserved, we note that it is unchanged by evolution under H_1, i.e. $\{\mathcal{G}, H_1\} = 0$ and for evolution under H_2 we find $\{\mathcal{G}, H_2\} = 2\mathbf{x}^{\mathrm{T}}\mathbf{V}\mathbf{p} - 2\mathbf{p}^{\mathrm{T}}\mathbf{V}\mathbf{x} = 0$ as $\mathbf{V}$ is symmetric.

Angle invariance is a direct consequence of unitarity.[85] To show this explicitly one can apply the transformation in Eq. (21) to Eq. (18) and then transform back, observing that evolution of the electronic positions and momenta are unaffected. The evolution of nuclear position in Eq. (16) is not directly dependent on the electronic variables and evolution of nuclear momenta in Eq. (19) is invariant to the transformation in Eq. (21).

Since the MInt algorithm is Hamiltonian evolution discretized by a symplectic method, there exists a modified Hamiltonian $\check{H}$ whose energy the algorithm conserves exponentially well over exponentially long time intervals.[80] The modified Hamiltonian, which is timestep-dependent, differs from the original Hamiltonian by the order of the algorithm,[80] so for the MInt algorithm

$$H(\mathbf{z}) - \check{H}(\mathbf{z}; \Delta t) = \mathcal{O}(\Delta t^2) \tag{C6}$$

and the MMST Hamiltonian $H(\mathbf{z})$ will be conserved for exponentially long times with fluctuations of $\mathcal{O}(\Delta t^2)$.

Appendix D: Liouvillian formalism

The algorithm in Eq. (14) in the Liouvillian representation is equivalent to

$$\Psi_{H,\Delta t} = e^{\mathcal{L}_1 \Delta t/2} e^{\mathcal{L}_2 \Delta t} e^{\mathcal{L}_1 \Delta t/2} \tag{D1}$$

where

$$\begin{aligned}\mathcal{L}_1 =& \{\cdot, H_1\} \\ =& \sum_k \frac{P_k}{\mu_{kk}} \frac{\partial}{\partial R_k}, \end{aligned} \tag{D2a}$$

$$\begin{aligned}\mathcal{L}_2 =& \{\cdot, H_2\} \\ =& -\sum_k \left\{ \frac{1}{2}(\mathbf{x} - i\mathbf{p})^{\mathrm{T}} \mathbf{V}_k(\mathbf{R})(\mathbf{x} + i\mathbf{p}) \right. \\ & \left. - \frac{1}{2}\mathrm{Tr}\left[\mathbf{V}_k(\mathbf{R})\right] \right\} \frac{\partial}{\partial P_k} \\ & + \mathbf{p}^{\mathrm{T}} \mathbf{V} \nabla_{\mathbf{x}} - \mathbf{x}^{\mathrm{T}} \mathbf{V} \nabla_{\mathbf{p}}. \end{aligned} \tag{D2b}$$

Note that each Liouvillian can be written as exact evolution under a Hamiltonian, and we follow the conventions of Zwanzig[83] and Ref. 80 by defining the Liouvillian without a prefactor of i.

An alternative scheme has been suggested for evolution in mapping variables which (in this notation) is[84]

$$\tilde{\Psi}_{H,\Delta t} = e^{\mathcal{L}_{\mathrm{el}}\Delta t/2} e^{\mathcal{L}_{\mathbf{P}}\Delta t/2} e^{\mathcal{L}_1 \Delta t} e^{\mathcal{L}_{\mathbf{P}}\Delta t/2} e^{\mathcal{L}_{\mathrm{el}}\Delta t/2} \tag{D3}$$

where $\mathcal{L}_1$ is defined in Eq. (D2a) and

$$\mathcal{L}_{\mathrm{el}} = + \mathbf{p}^{\mathrm{T}} \mathbf{V} \nabla_{\mathbf{x}} - \mathbf{x}^{\mathrm{T}} \mathbf{V} \nabla_{\mathbf{p}} \tag{D4a}$$

$$\begin{aligned}\mathcal{L}_{\mathbf{P}} =& -\sum_k \left\{ \frac{1}{2}(\mathbf{x} - i\mathbf{p})^{\mathrm{T}} \mathbf{V}_k(\mathbf{R})(\mathbf{x} + i\mathbf{p}) \right. \\ & \left. - \frac{1}{2}\mathrm{Tr}\left[\mathbf{V}_k(\mathbf{R})\right] \right\} \frac{\partial}{\partial P_k}. \end{aligned} \tag{D4b}$$

To compare these algorithms, we firstly note that the order of $\mathcal{L}_1$ and $\mathcal{L}_2$ in Eq. (D1) can be swapped without compromising the formal properties of the algorithm. Therefore one can define an alternative symplectic algorithm

$$\bar{\Psi}_{H,\Delta t} = e^{\mathcal{L}_2 \Delta t/2} e^{\mathcal{L}_1 \Delta t} e^{\mathcal{L}_2 \Delta t/2}, \tag{D5}$$

though this will be more computationally expensive than $\Psi_{H,\Delta t}$. We then note from Eq. (D2b) and Eq. (D4) that

$$\mathcal{L}_2 \equiv \mathcal{L}_{\mathrm{el}} + \mathcal{L}_{\mathbf{P}}. \tag{D6}$$

Consequently $\tilde{\Psi}_{H,\Delta t}$ is equivalent to making the approximation

$$e^{\mathcal{L}_2 \Delta t/2} \simeq e^{\mathcal{L}_{\rm el} \Delta t/2} e^{\mathcal{L}_{\mathbf{P}} \Delta t/2} \tag{D7}$$

to the symplectic propagator $\bar{\Psi}_{H,\Delta t}$. We therefore call $\bar{\Psi}_{H,\Delta t}$ the Split Liouvillian (SL) algorithm since it splits $e^{\mathcal{L}_2 \Delta t/2}$ into $e^{\mathcal{L}_{\rm el} \Delta t/2} e^{\mathcal{L}_{\mathbf{P}} \Delta t/2}$ (and $e^{\mathcal{L}_{\mathbf{P}} \Delta t/2} e^{\mathcal{L}_{\rm el} \Delta t/2}$).

The approximation in Eq. (D7) is clearly exact in the $\Delta t \to 0$ limit, and therefore $\tilde{\Psi}_{H,\Delta t}$ will be symplectic in this limit. It will also conserve electronic probability exactly for any time step like $\bar{\Psi}_{H,\Delta t}$ and $\Psi_{H,\Delta t}$.

However, $\mathcal{L}_{\rm el}$ and $\mathcal{L}_{\mathbf{P}}$ cannot in general be written as exact evolution under a Hamiltonian [cf. Eq. (D2)] and we show in appendix E that the SL algorithm is not in general symplectic for an arbitrary timestep.

Appendix E: Symplecticity properties of the MInt and SL algorithms

Here we confirm that the MInt algorithm is symplectic by explicitly evaluating Eq. (12) for each step of the algorithm. We also show that the SL algorithm in Eq. (D3) is not, in general, symplectic. For notational simplicity we present the results for one nuclear dof; further nuclear dof merely add more indices.

We first note that evolution under an arbitrary series of symplectic steps is also symplectic, since the monodromy matrix of the overall algorithm is the product of the monodromy matrices of the individual steps, and symplecticity can therefore be proven by applying Eq. (12) recursively. To prove that the MInt algorithm is symplectic it is therefore sufficient to prove

$$\mathbf{M}_{H_1}^{\rm T} \mathbf{J}^{-1} \mathbf{M}_{H_1} = \mathbf{J}^{-1} \tag{E1}$$

and

$$\mathbf{M}_{H_2}^{\rm T} \mathbf{J}^{-1} \mathbf{M}_{H_2} = \mathbf{J}^{-1} \tag{E2}$$

where $\mathbf{M}_{H_1}$ and $\mathbf{M}_{H_2}$ are the monodromy matrices associated with evolution under H_1 and H_2 respectively.

This manuscript was accepted by J. Chem. Phys. Click here to see the version of record.

1. Evolution under H_1

The monodromy matrix (for evolution with timestep $\Delta t/2$) is simply

$$\mathbf{M}_{H_1} = \begin{pmatrix} 1 & \mathbf{0}^{\mathrm{T}} & \Delta t/2m & \mathbf{0}^{\mathrm{T}} \\ \mathbf{0} & \mathbb{I} & \mathbf{0} & \mathbb{O} \\ 0 & \mathbf{0}^{\mathrm{T}} & 1 & \mathbf{0}^{\mathrm{T}} \\ \mathbf{0} & \mathbb{O} & \mathbf{0} & \mathbb{I} \end{pmatrix}. \tag{E3}$$

Simple matrix multiplication shows that this satisfies Eq. (E1).

2. Evolution under H_2

We firstly define

$$\mathsf{a} = -\mathbf{p}^{\mathrm{T}}\mathbf{E} + \mathbf{x}^{\mathrm{T}}\mathbf{F} \tag{E4a}$$

$$\mathsf{b} = -\frac{1}{2}\left[\mathbf{x}^{\mathrm{T}}\mathbf{E}'\mathbf{x} + \mathbf{p}^{\mathrm{T}}\mathbf{E}'\mathbf{p} - 2\mathbf{x}^{\mathrm{T}}\mathbf{F}'\mathbf{p}\right] + \frac{1}{2}\mathrm{Tr}\left[\mathrm{V}''\right]\Delta t \tag{E4b}$$

$$\mathsf{e} = -\mathbf{x}^{\mathrm{T}}\mathbf{E} - \mathbf{p}^{\mathrm{T}}\mathbf{F} \tag{E4c}$$

$$\mathsf{f} = \mathbf{C}'\mathbf{p} + \mathbf{D}'\mathbf{x} \tag{E4d}$$

$$\mathsf{g} = \mathbf{C}'\mathbf{x} - \mathbf{D}'\mathbf{p} \tag{E4e}$$

where the primes denote derivatives w.r.t. the nuclear coordinate, such that

$$\mathbf{M}_{H_2} = \begin{pmatrix} 1 & \mathbf{0}^{\mathrm{T}} & 0 & \mathbf{0}^{\mathrm{T}} \\ \mathsf{g} & \mathbf{C} & \mathbf{0} & -\mathbf{D} \\ \mathsf{b} & \mathsf{e} & 1 & \mathsf{a} \\ \mathsf{f} & \mathbf{D} & \mathbf{0} & \mathbf{C} \end{pmatrix} \tag{E5}$$

and

$$\mathbf{M}_{H_2}^{\mathrm{T}}\mathbf{J}^{-1}\mathbf{M}_{H_2} = \begin{pmatrix} 0 & -\mathsf{e} - \mathsf{g}^{\mathrm{T}}\mathbf{D} + \mathsf{f}^{\mathrm{T}}\mathbf{C} & -1 & -\mathsf{a} - \mathsf{g}^{\mathrm{T}}\mathbf{C} - \mathsf{f}^{\mathrm{T}}\mathbf{D} \\ -\mathbf{C}\mathsf{f} + \mathsf{e}^{\mathrm{T}} + \mathbf{D}\mathsf{g} & -\mathbf{C}\mathbf{D} + \mathbf{D}\mathbf{C} & \mathbf{0} & -\mathbf{C}\mathbf{C} - \mathbf{D}\mathbf{D} \\ 1 & \mathbf{0} & 0 & \mathbf{0} \\ \mathbf{D}\mathsf{f} + \mathsf{a}^{\mathrm{T}} + \mathbf{C}\mathsf{g} & +\mathbf{D}\mathbf{D} + \mathbf{C}\mathbf{C} & \mathbf{0} & +\mathbf{D}\mathbf{C} - \mathbf{C}\mathbf{D} \end{pmatrix}. \tag{E6}$$

This manuscript was accepted by J. Chem. Phys. Click here to see the version of record.

We firstly note that $\mathbf{CD} - \mathbf{DC} = \mathbb{O}$ since these matrices have the same eigenvectors and $\mathbf{CC} + \mathbf{DD} = \mathbb{I}$. We then define

$$\mathsf{h} := -\mathbf{C}\mathsf{f} + \mathsf{e}^{\mathrm{T}} + \mathbf{D}\mathsf{g} \tag{E7a}$$

$$\mathsf{j} := \mathbf{D}\mathsf{f} + \mathsf{a}^{\mathrm{T}} + \mathbf{C}\mathsf{g}, \tag{E7b}$$

such that Eq. (E6) reduces to

$$\mathbf{M}_{H_2}^{\mathrm{T}}\mathbf{J}^{-1}\mathbf{M}_{H_2} = \begin{pmatrix} 0 & -\mathsf{h}^{\mathrm{T}} & -1 & -\mathsf{j}^{\mathrm{T}} \\ \mathsf{h} & \mathbb{O} & \mathbf{0} & -\mathbb{I} \\ 1 & \mathbf{0} & 0 & \mathbf{0} \\ \mathsf{j} & \mathbb{I} & \mathbf{0} & \mathbb{O} \end{pmatrix}. \tag{E8}$$

To evaluate Eq. (E7) we define the matrices

$$\mathsf{A} := \mathbf{D}\mathbf{C}' - \mathbf{E} - \mathbf{C}\mathbf{D}' \tag{E9a}$$

$$\mathsf{B} := -(\mathbf{D}\mathbf{D}' - \mathbf{F} + \mathbf{C}\mathbf{C}'), \tag{E9b}$$

such that

$$\mathsf{h} \equiv \mathsf{A}\mathbf{x} + \mathsf{B}\mathbf{p} \tag{E10a}$$

$$\mathsf{j} \equiv -\mathsf{B}\mathbf{x} + \mathsf{A}\mathbf{p}. \tag{E10b}$$

In order to prove Eq. (E2), we must prove $\mathsf{h} \equiv \mathbf{0}$ and $\mathsf{j} \equiv \mathbf{0}$ $\forall$ $\mathbf{x}, \mathbf{p}$, which requires proving $\mathsf{A} \equiv \mathbb{O}$ and $\mathsf{B} \equiv \mathbb{O}$. As we shall see, it is mathematically convenient to prove this in the adiabatic basis, i.e. $\mathbf{S}^{\mathrm{T}}\mathsf{A}\mathbf{S} \equiv \mathbb{O}$ and $\mathbf{S}^{\mathrm{T}}\mathsf{B}\mathbf{S} \equiv \mathbb{O}$.

We find

$$\begin{aligned} \mathbf{S}^{\mathrm{T}}\mathsf{A}\mathbf{S} =& \boldsymbol{\Lambda}' t - \sin(\boldsymbol{\Lambda}\Delta t)\mathbf{S}^{\mathrm{T}}\mathbf{S}'\cos(\boldsymbol{\Lambda}\Delta t) \\ &+ \cos(\boldsymbol{\Lambda}\Delta t)\mathbf{S}^{\mathrm{T}}\mathbf{S}'\sin(\boldsymbol{\Lambda}\Delta t) - \boldsymbol{\Gamma} \end{aligned} \tag{E11}$$

such that

$$(\mathbf{S}^{\mathrm{T}}\mathsf{A}\mathbf{S})_{nm} = \boldsymbol{\Lambda}'_{nn}\delta_{nm}\Delta t + (\mathbf{S}^{\mathrm{T}}\mathbf{S}')_{nm}\sin(\lambda_{mn}\Delta t) - \boldsymbol{\Gamma}_{nm} \tag{E12}$$

To evaluate the $\mathbf{W}$ matrix in $\boldsymbol{\Gamma}$, we find from Eq. (B3)

$$\begin{aligned} \mathbf{W} =& \mathbf{S}^{\mathrm{T}}\left(\frac{\partial}{\partial R}\mathbf{S}\boldsymbol{\Lambda}\mathbf{S}^{\mathrm{T}}\right)\mathbf{S} \\ =& \mathbf{S}^{\mathrm{T}}\mathbf{S}'\boldsymbol{\Lambda} + \boldsymbol{\Lambda}' + \boldsymbol{\Lambda}\mathbf{S}'^{\mathrm{T}}\mathbf{S}. \end{aligned} \tag{E13}$$

This manuscript was accepted by J. Chem. Phys. Click here to see the version of record.

We also use the property that the nonadiabatic derivative coupling matrix $\mathbf{S}^{\mathrm{T}}\mathbf{S}'$ is antisymmetric, i.e. because $\mathbf{S}^{\mathrm{T}}\mathbf{S} = \mathbb{I}$, $\mathbf{S}'^{\mathrm{T}}\mathbf{S} + \mathbf{S}^{\mathrm{T}}\mathbf{S}' = \mathbb{O}$, and therefore

$$\mathbf{W}_{nm} = (\mathbf{S}^{\mathrm{T}}\mathbf{S}')_{nm}\lambda_{mn} + \mathbf{\Lambda}'_{nn}\delta_{nm}. \tag{E14}$$

Inserting this into Eq. (B6) we obtain

$$\mathbf{\Gamma}_{nm} = \begin{cases} \mathbf{\Lambda}'_{nn}\Delta t & n = m \\ -(\mathbf{S}^{\mathrm{T}}\mathbf{S}')_{nm}\sin(\lambda_{nm}\Delta t) & n \neq m \end{cases}, \tag{E15a}$$

$$\mathbf{\Xi}_{nm} = \begin{cases} 0 & n = m \\ [\cos(\lambda_{nm}\Delta t) - 1]\,(\mathbf{S}^{\mathrm{T}}\mathbf{S}')_{nm} & n \neq m \end{cases}. \tag{E15b}$$

Inserting Eq. (E15a) into Eq. (E12) shows that $\mathbf{S}^{\mathrm{T}}\mathsf{A}\mathbf{S} \equiv \mathbb{O}$ and therefore $\mathsf{A} \equiv \mathbb{O}$.

To prove that $\mathsf{B} = \mathbb{O}$, we find

$$(\mathbf{S}^{\mathrm{T}}\mathsf{B}\mathbf{S})_{nm} = -(\mathbf{S}^{\mathrm{T}}\mathbf{S}')_{nm}[\cos(\lambda_{nm}\Delta t) - 1] + \mathbf{\Xi}_{nm} \tag{E16}$$

since $\mathbf{S}^{\mathrm{T}}\mathbf{S}$ is skew-symmetric (see above) then the diagonal elements of this will vanish, and the off-diagonal elements also vanish by Eq. (E15b), such that $\mathsf{B} \equiv \mathbb{O}$. Consequently $\mathsf{h} = \mathbf{0}$ by Eq. (E10a) and $\mathsf{j} = \mathbf{0}$ by Eq. (E10b), proving that evolution under H_2 is symplectic. Combining this with section E 1 proves that $\Psi_{H,\Delta t}$ (the MInt algorithm) and $\bar{\Psi}_{H,\Delta t}$ are symplectic for any timestep, confirming our earlier statement of symplecticity which was based upon contructing a method by Hamiltonian splitting.[80]

3. The SL algorithm

As noted above, the only difference between $\bar{\Psi}_{H,\Delta t}$ (which we have just proven to be symplectic) and the SL algorithm $\tilde{\Psi}_{H,\Delta t}$ is the approximation in Eq. (D7). We therefore seek to determine whether successive evolution under $\mathcal{L}_{\mathrm{el}}$ then $\mathcal{L}_{\mathbf{P}}$ is symplectic. The monodromy matrix associated with nuclear momentum evolution (for timestep Δt) is

$$\mathbf{M}_{\mathbf{P}} = \begin{pmatrix} 1 & \mathbf{0}^{\mathrm{T}} & 0 & \mathbf{0}^{\mathrm{T}} \\ \mathbf{0} & \mathbf{1} & \mathbf{0} & \mathbf{0} \\ \tilde{\mathsf{b}} & -\mathbf{q}^{\mathrm{T}}\mathbf{V}'\Delta t & 1 & -\mathbf{p}^{\mathrm{T}}\mathbf{V}'\Delta t \\ \mathbf{0} & \mathbf{0} & \mathbf{0} & \mathbf{1} \end{pmatrix} \tag{E17}$$

This manuscript was accepted by J. Chem. Phys. Click here to see the version of record.

and the matrix associated with electronic evolution only is

$$\mathbf{M}_{\mathrm{el}} = \begin{pmatrix} 1 & \mathbf{0}^{\mathrm{T}} & 0 & \mathbf{0}^{\mathrm{T}} \\ \mathsf{g} & \mathbf{C} & \mathbf{0} & -\mathbf{D} \\ 0 & \mathbf{0}^{\mathrm{T}} & 1 & \mathbf{0}^{\mathrm{T}} \\ \mathsf{f} & \mathbf{D} & \mathbf{0} & \mathbf{C} \end{pmatrix} \tag{E18}$$

where f and g are defined in Eq. (E4) and

$$\tilde{\mathsf{b}} := -\frac{1}{2}\left(\mathbf{x}^{\mathrm{T}}\mathbf{V}''\mathbf{x} + \mathbf{p}^{\mathrm{T}}\mathbf{V}''\mathbf{p} - \mathrm{Tr}\left[\mathbf{V}''\right]\right). \tag{E19}$$

We firstly note that $\det|\mathbf{M}_{\mathbf{P}}| \equiv 1$ and $\det|\mathbf{M}_{\mathrm{el}}| \equiv 1$, which means that the SL algorithm will satisfy Liouville's theorem, a necessary but not sufficient criterion for symplecticity.

However,

$$\mathbf{M}_{\mathbf{P}}^{\mathrm{T}}\mathbf{J}^{-1}\mathbf{M}_{\mathbf{P}} = \begin{pmatrix} 0 & \mathbf{x}^{\mathrm{T}}\mathbf{V}'\Delta t & -1 & \mathbf{p}^{\mathrm{T}}\mathbf{V}'\Delta t \\ -\mathbf{V}'\mathbf{x}\Delta t & \mathbb{O} & \mathbf{0} & -\mathbb{I} \\ 1 & \mathbf{0}^{\mathrm{T}} & 0 & \mathbf{0}^{\mathrm{T}} \\ -\mathbf{V}'\mathbf{p}\Delta t & \mathbb{I} & \mathbf{0} & \mathbb{O} \end{pmatrix} \tag{E20}$$

so evolution under $\mathcal{L}_{\mathbf{P}}$ is not symplectic unless $\mathbf{V}' = 0$ (the diabatic matrix has no nuclear dependence). Furthermore,

$$\begin{aligned} &\mathbf{M}_{\mathrm{el}}^{\mathrm{T}}\mathbf{J}^{-1}\mathbf{M}_{\mathrm{el}} \\ &= \begin{pmatrix} 0 & -\mathsf{g}^{\mathrm{T}}\mathbf{D} + \mathsf{f}^{\mathrm{T}}\mathbf{C} & -1 & -\mathsf{g}^{\mathrm{T}}\mathbf{C} - \mathsf{f}^{\mathrm{T}}\mathbf{D} \\ -\mathbf{C}\mathsf{f} + \mathbf{D}\mathsf{g} & \mathbf{0} & \mathbf{0} & -\mathbb{I} \\ \mathbf{1} & \mathbf{0} & 0 & \mathbf{0} \\ \mathbf{D}\mathsf{f} + \mathbf{C}\mathsf{g} & \mathbb{I} & \mathbf{0} & \mathbf{0} \end{pmatrix} \\ &\equiv \begin{pmatrix} 0 & \mathsf{e} & -1 & \mathsf{a} \\ -\mathsf{e}^{\mathrm{T}} & \mathbf{0} & \mathbf{0} & -\mathbb{I} \\ \mathbf{1} & \mathbf{0} & 0 & \mathbf{0} \\ -\mathsf{a}^{\mathrm{T}} & \mathbb{I} & \mathbf{0} & \mathbf{0} \end{pmatrix} \end{aligned} \tag{E21}$$

where we have exploited Eq. (E7) and the earlier proofs that $\mathsf{h} \equiv \mathbf{0}$ and $\mathsf{j} \equiv \mathbf{0}$. In general $\mathsf{a} \neq \mathbf{0}$ and $\mathsf{e} \neq \mathbf{0}$, so evolution under $\mathcal{L}_{\mathrm{el}}$ is not symplectic.

We also consider combined evolution of both $\mathcal{L}_{\mathbf{P}}$ and $\mathcal{L}_{\mathrm{el}}$ in order to compare the SL and MInt algorithms on an equal footing and show that the combination of steps does not

This manuscript was accepted by J. Chem. Phys. Click here to see the version of record.

lead to cancellation of errors which restores symplecticity. We consider evolution under $\mathcal{L}_{\mathbf{P}}$ followed by $\mathcal{L}_{\mathrm{el}}$ (the fourth and fifth steps of the SL algorithm), since evolution under $\mathcal{L}_{\mathbf{P}}$ first does not change the electronic dofs subsequently used in $\mathbf{M}_{\mathrm{el}}$ and therefore leads to simpler algebra. We find

$$\mathbf{M}_{\mathrm{el}}\mathbf{M}_{\mathbf{P}} = \begin{pmatrix} 1 & \mathbf{0} & 0 & \mathbf{0} \\ \mathsf{g} & \mathbf{C} & \mathbf{0} & -\mathbf{D} \\ \tilde{\mathsf{b}} & -\mathbf{x}^{\mathrm{T}}\mathbf{V}'\Delta t & 1 & -\mathbf{p}^{\mathrm{T}}\mathbf{V}'\Delta t \\ \mathsf{f} & -\mathbf{D} & \mathbf{0} & \mathbf{C} \end{pmatrix} \tag{E22}$$

comparison with Eq. (E5) leads us to define

$$\tilde{\mathsf{a}} := -\mathbf{p}^{\mathrm{T}}\mathbf{V}'\Delta t \tag{E23a}$$

$$\tilde{\mathsf{e}} := -\mathbf{x}^{\mathrm{T}}\mathbf{V}'\Delta t \tag{E23b}$$

such that

$$\mathbf{M}_{\mathrm{el}}\mathbf{M}_{\mathbf{P}} = \begin{pmatrix} 1 & \mathbf{0} & 0 & \mathbf{0} \\ \mathsf{g} & \mathbf{C} & \mathbf{0} & -\mathbf{D} \\ \tilde{\mathsf{b}} & \tilde{\mathsf{e}} & 1 & \tilde{\mathsf{a}} \\ \mathsf{f} & -\mathbf{D} & \mathbf{0} & \mathbf{C} \end{pmatrix} \tag{E24}$$

Comparison with section E 2 means that $\mathbf{M}_{\mathbf{P}}^{\mathrm{T}}\mathbf{M}_{\mathrm{el}}^{\mathrm{T}}\mathbf{J}^{-1}\mathbf{M}_{\mathrm{el}}\mathbf{M}_{\mathbf{P}} = \mathbf{J}^{-1}$ if and only if $\tilde{\mathsf{a}} \equiv \mathsf{a}$ and $\tilde{\mathsf{e}} \equiv \mathsf{e}$, since the $\tilde{\mathsf{b}}$ term cancels out. Expanding these conditions in coefficients of $\mathbf{x}$ and $\mathbf{p}$ leads to the conditions

$$\mathbf{E} \stackrel{?}{=} \mathbf{V}'\Delta t, \tag{E25a}$$

$$\mathbf{F} \stackrel{?}{=} \mathbf{0}. \tag{E25b}$$

Evaluating these in the adiabatic basis (as above) gives

$$\mathbf{S}^{\mathrm{T}}(\mathbf{E} - \mathbf{V}'\Delta t)\mathbf{S} = \mathbf{\Gamma} - \mathbf{W}\Delta t, \tag{E26a}$$

$$\mathbf{S}^{\mathrm{T}}\mathbf{F}\mathbf{S} = \mathbf{\Xi}, \tag{E26b}$$

and evaluating these elementwise in powers of Δt gives

$$(\mathbf{\Gamma} - \mathbf{W}\Delta t)_{nm} = \begin{cases} 0 & n = m \\ -\frac{\lambda_{nm}^2}{3!}\Delta t^3 W_{nm} + \mathcal{O}(\Delta t^5) & n \neq m \end{cases}, \tag{E27a}$$

$$\mathbf{\Xi}_{nm} = \begin{cases} 0 & n = m \\ \frac{\lambda_{nm}}{2!}\Delta t^2 W_{nm} + \mathcal{O}(\Delta t^4) & n \neq m \end{cases}. \tag{E27b}$$

This means that $(\tilde{\mathsf{e}} - \mathsf{e})$ and $(\tilde{\mathsf{a}} - \mathsf{a})$ will be $\mathcal{O}(\Delta t^2)$. The SL algorithm will therefore be symplectic in the $\Delta t \to 0$ limit (as noted above) but for an arbitrary timestep will not be symplectic. Consequently the energy is likely to drift, though the extent of the drift may be small if the adiabatic states are closely separated and there is little off-diagonal coupling in the adiabatic basis (i.e. $\lambda_{nm} W_{nm} \Delta t^2 \ll 1$). We also observe that the combination $\mathbf{M}_{\mathrm{el}}\mathbf{M}_{\mathbf{P}}$ is symplectic to one higher order in time to $\mathbf{M}_{\mathrm{el}}$ or $\mathbf{M}_{\mathbf{P}}$ which from Eq. (E20) and Eq. (E21) will be symplectic to $\mathcal{O}(\Delta t)$.

REFERENCES

[1]W. Domcke and D. R. Yarkony, Annu. Rev. Phys. Chem. **63** (2012), 325.

[2]Y. R. Reese and D. G. Nocera, Annu. Rev. Biochem. **78** (2009), 673.

[3]H. B. Gray and J. R. Winkler, Annu. Rev. Biochem. **65** (1996), 537.

[4]H. B. Gray and J. R. Winkler, Proc. Natl. Acad. Sci. U.S.A. **102** (2005), 3534.

[5]S. Hammes-Schiffer and A. A. Stuchebrukhov, Chem. Rev. **110** (2010), 6939.

[6]K. Golibrzuch, N. Bartels, D. J. Auerbach and A. M. Wodtke, Annu. Rev. Phys. Chem. **66** (2015), 399.

[7]B. C. Kruger, N. Bartels, C. Bartels, A. Kandratsenka, J. C. Tully and A. M. Wodtke, J. Phys. Chem. C **119** (2015), 3268.

[8]M. Topaler and N. Makri, J. Phys. Chem. **100** (1996), 4430.

[9]M. H. Beck, A. Jäckle, G. A. Worth and H. D. Meyer, Phys. Rep. **324** (2000), 1.

[10]T. J. H. Hele and N. Ananth, Faraday Discuss. **195** (2016), 269.

[11]S. J. Cotton and W. H. Miller, Faraday Discuss. **195** (2016), 9.

[12]R. Kapral, Annu. Rev. Phys. Chem. **57** (2006), 129.

[13]A. Donoso and C. C. Martens, J. Phys. Chem. A **102** (1998), 4291.

[14]C. C. Martens, Chem. Phys. **481** (2016), 60.

[15]J. C. Tully, J. Chem. Phys. **93** (1990), 1061.

[16]O. V. Prezhdo and P. J. Rossky, J. Chem. Phys. **107** (1997), 825.

[17]A. W. Jasper, S. N. Stechmann and D. G. Truhlar, J. Chem. Phys. **116** (2002), 5424.

[18]M. F. Herman, J. Chem. Phys. **103** (1995), 8081.

[19]Y. Wu and M. F. Herman, J. Chem. Phys. **127** (2007), 044109.

[20]B. R. Landry and J. E. Subotnik, J. Chem. Phys. **137** (2012), 22A513.

[21]T. Zimmermann and J. Vanicek, J. Chem. Phys. **141** (2014), 134102.

[22]A. J. White, V. N. Gorshkov, S. Tretiak and D. Mozyrsky, J. Chem. Phys. **143** (2015), 014115.

[23]I. R. Craig and D. E. Manolopoulos, J. Chem. Phys. **121** (2004), 3368.

[24]S. Habershon, D. E. Manolopoulos, T. E. Markland and T. F. M. III, Ann. Rev. Phys. Chem. **64** (2013), 387, pMID: 23298242.

[25]T. J. H. Hele, M. J. Willatt, A. Muolo and S. C. Althorpe, J. Chem. Phys. **142** (2015), 134103.

[26]T. J. H. Hele, M. J. Willatt, A. Muolo and S. C. Althorpe, J. Chem. Phys. **142** (2015), 191101.

[27]T. J. H. Hele, Mol. Phys. **13** (2017), 1435.

[28]G. A. Voth, Path-Integral Centroid Methods in Quantum Statistical Mechanics and Dynamics, Adv. Chem. Phys., John Wiley & Sons, Inc. (1996).

[29]P. Shushkov, R. Li and J. C. Tully, J. Chem. Phys. **137** (2012), 22A549/1.

[30]N. Ananth, J. Chem. Phys. **139** (2013), 124102.

[31]J. R. Duke and N. Ananth, J. Phys. Chem. Lett. **6** (2015), 4219.

[32]J. R. Duke and N. Ananth, Faraday Discuss. **195** (2016), 253.

[33]F. A. Shakib and P. Huo, J. Phys. Chem. Lett. **8** (2017), 3073.

[34]J.-L. Liao, and G. A. Voth, J. Phys. Chem. B **106** (2002), 8449.

[35]T. F. Miller III, J. Chem. Phys. **129** (2008), 194502.

[36]A. R. Menzeleev, N. Ananth and T. F. Miller III, J. Chem. Phys. **135** (2011), 074106.

[37]N. Ananth and T. F. Miller III, J. Chem. Phys. **133** (2010), 234103.

[38]A. R. Menzeleev, F. Bell and T. F. Miller III, J. Chem. Phys. **140** (2014), 064103.

[39]M. F. Herman and E. Kluk, Chemical Physics **91** (1984), 27.

[40]W. H. Miller, J. Phys. Chem. A **105** (2001), 2942.

[41]M. Thoss and H. Wang, Annu. Rev. Phys. Chem. **55** (2004), 299.

[42]K. G. Kay, J. Chem. Phys. **100** (1994), 4377.

[43]K. G. Kay, Annu. Rev. Phys. Chem. **56** (2005), 255.

[44]X. Sun and W. H. Miller, J. Chem. Phys. **106** (1997), 6346.

[45]E. A. Coronado, V. S. Batista and W. H. Miller, J. Chem. Phys. **112** (2000), 5566.

[46]N. Ananth, C. Venkataraman and W. H. Miller, J. Chem. Phys. **127** (2007), 084114.

[47]W. H. Miller, J. Phys. Chem. A **113** (2009), 1405.

[48]G. Tao, J. Phys. Chem. A **117** (2013), 5821.

[49]F. Agostini, S. K. Min and E. K. U. Gross, Ann. Phys. (Berlin) 527 **527** (2015), 546.

[50]H. Wang, X. Sun and W. H. Miller, J. Chem. Phys. **108** (1998), 9726.

[51]X. Sun, H. Wang and W. H. Miller, J. Chem. Phys. **109** (1998), 4190.

[52]J. Liu, Int. J. Quantum Chem. (2015), published online, doi: 10.1002/qua.24872.

[53]Q. Shi and E. Geva, J. Phys. Chem. A **108** (2004), 6109.

[54]N. Makri, J. Phys. Chem. B **106** (2002), 8390.

[55]J. Kegerreis and N. Makri, J. Comput. Chem. **28** (2007), 818.

[56]N. Makri and K. Thompson, Chem. Phys. Lett. **291** (1998), 101.

[57]X. Sun and W. H. Miller, J. Chem. Phys. **110** (1999), 6635.

[58]W. H. Miller, Faraday Discuss. **110** (1998), 1.

[59]H. Wang, M. Thoss and W. H. Miller, J. Chem. Phys. **112** (2000), 47.

[60]J. Shao and N. Makri, J. Phys. Chem. A **103** (1999), 7753.

[61]R. Gelavert, X. Gimenez, M. Thoss, H. Wang and W. H. Miller, J. Chem. Phys. **114** (2001), 2572.

[62]K. Thompson and N. Makri, Phys. Rev. E **59** (1999), R4729.

[63]S. V. Antipov, Z. Ye and N. Ananth, J. Chem. Phys. **142** (2015), 184102.

[64]M. S. Church, S. V. Antipov and N. Ananth, J. Chem. Phys. **146** (2017), 234104.

[65]E. A. Coronado, J. Xing and W. H. Miller, Chem. Phys. Lett. **349** (2001), 521 .

[66]V. S. Filinov, Nuc. Phys. B **271** (1986), 717.

[67]N. Makri and W. H. Miller, Chem. Phys. Lett. **139** (1987), 10.

[68]N. Makri and W. H. Miller, J. Chem. Phys. **89** (1988), 2170.

[69]B. W. Spath and W. H. Miller, J. Chem. Phys. **104** (1996), 95.

[70]B. W. Spath and W. H. Miller, Chem. Phys. Lett. **262** (1996), 486.

[71]M. F. Herman, Chem. Phys. Lett. **275** (1997), 445.

[72]A. R. Walton and D. E. Manolopoulos, Mol. Phys. **87** (1996), 961.

[73]X. Sun and W. H. Miller, J. Chem. Phys. **108** (1998), 8870.

[74]M. Thoss, H. Wang and W. H. Miller, J. Chem. Phys. **114** (2001), 9220.

[75]M. Spanner, V. S. Batista and P. Brumer, J. Chem. Phys. **122** (2005), 084111.

[76]H. D. Meyer and W. H. Miller, J. Chem. Phys. **70** (1979), 3214.

[77]G. Stock and M. Thoss, Phys. Rev. Lett. **78** (1997), 578.

[78]A. Nitzan, Chemical Dynamics in Condensed Phases, Oxford University Press, New York

(2006).

[79]M. E. Tuckerman, Statistical Mechanics: Theory and Molecular Simulation, Oxford University Press (2010).

[80]B. Leimkuhler and S. Reich, Simulating Hamiltonian Dynamics, Cambridge University Press (2004).

[81]T. F. Miller III, M. Eleftheriou, P. Pattnaik, A. Ndirango, D. Newns and G. J. Martyna, J. Chem. Phys. **116** (2002), 8649.

[82]M. Tuckerman, B. J. Berne and G. J. Martyna, J. Chem. Phys. **97** (1992), 1990.

[83]R. Zwanzig, Nonequilibrium statistical mechanics, Oxford University Press, New York (2001).

[84]J. O. Richardson, P. Meyer, M.-O. Pleinert and M. Thoss, Chem. Phys. **482** (2016), 124.

[85]H.-D. Meyer and W. H. Miller, J. Chem. Phys. **70** (1979), 3214.

[86]F. Pan and G. Tao, J. Chem. Phys. **138** (2013), 091101.

[87]D. J. Tannor, Introduction to Quantum Mechanics: A Time-Dependent Perspective, University Science Books (2007).

[88]M. L. Brewer, J. S. Hulme and D. E. Manolopoulos, J. Chem. Phys. **106** (1997), 4832.

[89]T. J. H. Hele, An electronically non-adiabatic generalization of ring polymer molecular dynamics, MChem thesis, Exeter College, University of Oxford (2011).

[90]J. R. Magnus, Econometr. Theor. **1** (1985), 179.